NOTE: This manuscript is **not** peer reviewed. Currently the manuscript is under review in Chemical Geology.

Flux Modulated Magmatic Architecture in Continental Magmatic Arcs

Charles Lewis[1†], Shanaka de Silva[1]

[1]Oregon State University; College of Earth, Ocean, and Atmospheric Sciences (CEOAS); 104 CEOAS Admin Bldg. Corvallis, OR 97331

[†] Corresponding Author

Abstract

Petrochronology of the magmatic reservoir that underpinned the Chaxas Volcanic Complex for the duration of its 8.59 – 1.24 Ma lifecycle reveals that magmatic architecture can be regulated by magmatic flux. Modulation of the magmatic reservoir was controlled via two distinct flux regimes during the Pre-Chaxas and Chaxas Complex stages of the Chaxas Volcanic Complex, emphasizing the dynamic nature of magmatic systems that characterize continental magmatic systems. Although Pre-Chaxas eruptions began at 5.44 Ma, intrusions were emplaced as early as 8.59 Ma during the waxing stage of the APVC flare-up. The Pre-Chaxas stage climaxed with the APVC flare-up, resulting in catastrophic eruption of the Puripicar Ignimbrite (PPI) at 4.18 Ma. The overdispersed zircon age spectrum in the PPI spans several Myr, recording the long episodic history of the composite Pre-Chaxas system. Thermal models predict that the preceding 500 kyr episode to the PPI occurred under a magmatic flux of $>5 \times 10^{-3}$ km^3/yr with a total intrusive volume of ~ 5300 km^3, leaving approximately 4800 km^3 of remnant mush. High Zr/Hf zircons in evolved Pre-Chaxas eruptions record assimilation of crustal material during this stage. Starting at 3.54 Ma, smaller predominantly effusive eruptions built the Chaxas Complex. Age spectra from the Chaxas Complex reveal shorter time domains within discrete melt batches injected into Pre-Chaxas cumulates. Thermal modeling suggests maximum fluxes of $<7 \times 10^{-4}$ km^3/yr and ~ 1500 km^3 of intrusions. The petrochronologic record from the Chaxas Volcanic Complex demonstrates that the construction of composite plutons over millions of years is the result of dynamic magmatic systems that respond to changes in magmatic flux.

Introduction

The tempo of volcanic activity and magmatic assemblage within upper crustal reservoirs beneath continental volcanic arcs is controlled by flux rates into the reservoirs (National Academies of Sciences, Engineering, and Medicine, 2017). This is most obviously manifested during regional ignimbrite flare-ups defined as periods of anomalously vigorous silicic volcanic activity in a relatively short period of time with respect to the lifecycle of the orogen, during which tens of thousands of cubic kilometers of magma is erupted at volcanic fluxes of ~ 10^2 – 10^3 km^3 yr^{-1} (Bertin et al., 2023; Coney and Reynolds, 1977). The volcanic record of such flare-ups consists of spatially dense clusters of calderas that source eruptions with volumes of 10^2 – 10^3 s km^3 and leave behind extensive upper crustal plutonic complexes, (Best et al., 2016; Lipman et al., 1978). Resolving the spatiotemporal organization of such large silicic reservoirs through evaluation of crystallization histories is necessary for describing the secular evolution of Earth's crust, assembly and evolution of granitic batholiths, and the run-up to eruptions. Key to achieving this goal is temporally resolving changes to magmatic systems now commonly being achieved through combined geochronology and petrology – so called petrochronology (Schmitt and Vazquez, 2017; Tavazzani et al., 2023). In idealized and some rare natural cases magmatic systems appear to behave predictably, showing monotonic cooling trends during construction of plutonic complexes (Samperton et al., 2017). On the contrary, field, geochronological, and geochemical data gathered from many volcanic and plutonic systems are not uniformly predictable but rather record a complex intrusion history accompanied by high geochemical variability (Eddy et al., 2022). Deconvolution of magmatic processes that occurred prior to eruption must then be traced through detailed petrologic studies of the crystal cargo that serve as faithful petrochronologic records during their growth (Vazquez and Reid 2004). Various magmatic processes including but not limited to incremental emplacement of chemically discrete magma batches (Coleman et al., 2004), assimilation (Grant et al., 2009), cannibalization (Schmitt et al., 2010), and rapid silicic melt extraction events (Lewis et al., 2022; Schaen et al., 2021) all contribute to and induce thermal and chemical changes to large magmatic systems and their host rocks. Petrochronology has demonstrated potential to unravel this complex matrix of building blocks and processes through which magmatic architectures result.

Application of U-Pb zircon petrochronology to assessment of magma assembly has revealed a myriad of time domains (Schmitt et al., 2023). Depending on the size of the magmatic system, estimated durations of magmatism at a single center can extend from one to ten million years (Matzel et al., 2006), whereas melt presence in a reservoir can range from approximately one million years (Kaiser et al., 2017) down to only tens of thousands or hundreds of thousands of years (Paterson et al., 2011). In magmatic systems with prolonged age spectra, discrete magmatic events result in multimodal distributions that are the hallmark of zircon petrochronology, though assigning accurate timing between magmatic events is often difficult due to densely overlapping uncertainties. Resolution of these events between one another can be facilitated by statistical resolution of discrete age subpopulations within multimodal age spectra (Sambridge and Compston, 1994). The protracted U-Pb zircon petrochronologic record of the Chaxas Volcanic Complex is used here to assess the construction of a magmatic system that temporally straddles the waxing and waning of the ignimbrite flare-up that built the Altiplano Puna Volcanic Complex (APVC) of the Central Andes.

Petrochronology of the Chaxas Volcanic Complex reveals the prolonged construction and dynamic architecture that is modulated by the regional magmatic flux.

Continental Magmatic Arc Context

Altiplano-Puna Volcanic Complex

Straddling the triple junction of Chile, Bolivia, and Argentina, the APVC is a 70,000 km^2 ignimbrite-caldera plateau at the transition from the Altiplano to the Puna segments of the Central Andean Plateau. Constructed between approximately 10 and 1 Ma, the APVC is notable for its dominance of isotopically enriched, high-K dacite and subordinate rhyolite ignimbrites that are typically sourced from large caldera structures (Kern et al., 2016; Salisbury et al., 2011), nine of which have supereruption scale volumes of ≥ 500 km^3. The silicic magmas that erupted during the APVC flare-up are the result of extensive assimilation-fractional crystallization from subduction-related basaltic parental magmas during their journey through 70 to 80 km thickness of the sub-Andean crust (Burns and de Silva, 2023; Kay et al., 2010). The APVC is underlain by the Altiplano-Puna Magma Body, a seismic low-velocity zone extending from 15-30 km depth, in which a region approximately 500,000 km^3 with up to 20% partial melt has been interpreted (Pritchard et al., 2018; Ward et al., 2014). The APMB is inferred to be the andesitic parental reservoir to the 8 to 2 km deep dacitic magma bodies that feed the APVC eruptions (Grocke et al., 2017; Kaiser et al., 2017). Volcanic output during the flare-up imply remarkable magma addition rates of ~ 70 km^3 / km arc / million years (de Silva and Kay, 2018; Bertin, 2023); substantially higher than the steady state estimate of 20 km^3 / km arc / million years (Jicha and Jagoutz, 2015).

Chaxas Volcanic Complex

The Chaxas Volcanic Complex was built in two temporally distinct stages (Table 1; Lewis et al., 2025). The Pre-Chaxas stage began with the 5.4 Ma Agua Perdida rhyolite (APR), followed by the ≥ 500 km^3 4.18 Ma Puripicar ignimbrite (PPI), and the 3.73 Ma Embaucador Rhyolite (ER). The APR and ER are crystal poor (~10 % crystallinity) rhyolites with a modal mineralogy comprised of plagioclase > quartz > biotite; the ER contains sanidine. The PPI is a relatively well-studied “monotonous” crystal-rich dacite that has attracted numerous workers due to its preservation along the Andean front (de Silva, 1989; Kern et al., 2016; Salisbury et al., 2011). The 3.54 – 1.24 Ma Chaxas Complex comprises a series of endogenous domes and block and ash flows (B&As), small pyroclastic density currents (PDCs) and pyroclastic fallouts (PF) at the southwestern margin of the APVC (Figure 1). A thin pyroclastic fallout outcrops at the base of the Chaxas Complex (PFI). The 3.7 km^3 Cerro Chaxas (CC) is the southernmost dome that was emplaced in the Chaxas dome complex at 1.86 Ma. CC is surrounded by a fan of B&As that erupted from 2.75 – 1.83 Ma emplaced during phases of growth and collapse, referred to as the Youngest (YBA), Middle (MBA), and Oldest B&A (OBA). These are overlain by a small PDC known as the Final del Agua Rhyolite (FAR). Lewis et al. (2025) have demonstrated that the source “caldera” for the PPI is hidden by overlying lavas of younger episodes associated with the Chaxas Complex. All lithologies erupted at the Chaxas Volcanic Complex are chemically typical of the APVC and are cogenetic and consanguineous.

Methodology

Zircon U-Pb Ages

U-Pb zircon ages collected at Oregon State University (OSU) by Laser Ablation – Quadrupole – Inductively Coupled Plasma – Mass Spectrometry (LA-Q-ICP-MS) and LA-Multicollector-ICP-MS (LA-MC-ICP-MS) have been previously reported (Lewis et al., 2025) and the methodology is reiterated in supplementary file 2. All uncertainties were propagated according to standard protocol (Horstwood et al., 2016) and are reported at 2s. Instrumental parameters, U-Pb data, and standard reproducibility are tabulated in the supplementary materials.

Reported U-Pb dates below includes the difference between the oldest and youngest dates (t_{tot}), excluding xenocrysts. Eruption ages are also not reported as dates as they have been previously defined (Lewis et al. 2025; Table 1).

Zircon Trace Elements and Ti-in-Zircon Temperatures

Trace element concentrations in zircon were determined using the laser system and parameters described for LA-Q-ICP-MS U-Pb geochronology. CL-images were used to select spots in the same growth zones that were selected for U-Pb geochronology given the amount of space available. This allows for direct analysis of the relationship between age and zircon trace element abundance (e.g., Farina et al. 2024). Reference materials were analyzed in blocks every 20 analyses. All data were reduced using LaserTRAM-DB (Lubbers et al., 2025) with ^{29}Si as an internal standard and an assumed 32.8 wt % SiO_2. GSE-1G was used as a primary standard given the high abundance of trace element concentrations. Secondary standard data, all unknowns, and a full list of analytes are reported in supplementary file 1.

Ti-in-zircon temperatures were calculated according to Ferry and Watson (2007). Quartz phenocrysts are present in the lithologies of all silicic rocks discussed here and so SiO_2 activity is assumed to be unity. TiO_2 activity is assumed to take on the nominal value of 0.6. This value is the intermediate value of ilmenite saturated silicic magmas (~ 0.5) and Ti-magnetite saturated silicic magmas (~ 0.7), both of which are present in the studied magmas and it can thus be reasonably assumed that the TiO_2 activity was buffered to ~ 0.6.

<u>Results</u>

Zircon U-Pb Dates

PPI dates are extremely overdispersed (MSWD = 8.4) with dates ranging from 8.7 ± 0.5 Ma to 4.4 ± 1.2 Ma (Figure 2), defining the largest t_{tot} of all eruptions in this study at 4.4 million years. This duration extends from the first major pulse of the APVC flare-up at ca. 8.5 Ma to the second at ca. 4 Ma.

CC dome clasts and B&As have the tightest distribution of U-Pb dates amongst those in eruptions studied here. YBA U-Pb zircon dates are moderately overdispersed (MSWD = 3.9) with a date range of 1.8 ± 0.3 Ma to 4.3 ± 2.7 Ma (t_{tot}: 2.5 million years). CC U-Pb zircon dates have a relatively short t_{tot} of 1.0 million years (1.9 ± 0.1 Ma to 2.8 ± 0.4 Ma), excepting a single date that overlaps with Pre-Chaxas U-Pb dates at 6.3 ± 0.4 Ma. Zircon U-Pb dates in MBA share a similar range to CC. Dates ranging between 2.2 ± 0.9 Ma and 2.7 ± 1.3 Ma form an evenly dispersed age spectra (MSWD = 0.6; n = 39) across a t_{tot} of 500 thousand years. Similar to CC there is a single date outside of this range at 4.7 ± 0.3 Ma. OBA zircon show more overdispersion in their dates than zircon from other dome rocks (MSWD = 6.12; n = 17) with a relatively large t_{tot} of 2.2 million years, defined by dates ranging from 2.7 ± 0.5 Ma to 5.0 ± 0.5 Ma. Most of the OBA U-Pb dates overlap with ER and PPI dates.

Rhyolites have overdispersed zircon U-Pb dates. PFI dates range from 3.5 ± 0.5 Ma to 5.8 ± 1.6 Ma (t_{tot}: 2.3 million years), defining an overdispersed set of dates (MSWD = 13.3; n = 16) that overlaps almost entirely with the ER and PPI. ER dates span nearly the range of the PPI with a range from 3.7 ± 0.3 Ma to 7.3 ± 0.8 Ma (t_{tot}: 3.5 million years) and are also overdispersed (MSWD = 13.3; n = 72). FAR dates also have a large t_{tot} from an overdispersed dataset (MSWD = 37.1; n = 10) though three distinct subpopulations are clearly present (Figure

2). APR has an overdispersed dataset (MSWD = 3.6; n = 23) and a date range restricted to the second pulse of the APVC flare-up from 5.4 ± 0.4 Ma to 6.8 ± 0.5 Ma.

Trace Elements

The PPI has very variable zircon trace elements (ZTE). Th/U values negatively covary with REE patterns. Zr/Hf in PPI zircons define two groups of high Zr/Hf zircons (Zr/Hf 48.8 – 55.3) and low Zr/Hf zircons (Zr/Hf: 36.4 – 43.9). High Zr/Hf PPI zircons are positively correlated with Ti-in zircon temperatures that range from 731 °C to 847 °C (Figure 3). Low Zr/Hf PPI zircons record low Ti-in-zircon temperatures (665 °C to 757 °C). PPI ZTE have a large Eu anomaly range (0.6 – 0.1) and the largest range of U concentrations of all eruptions (Figure 4).

CC dome clasts and B&As have more subtle ZTE variation than the PPI and have low U concentrations. Yb/Dy negatively covaries with Th/U values, although MBA ZTE shows a fairly restricted range in these ratios and steep Eu anomalies. Zr/Hf in YBA and MBA are low (Zr/Hf: 39 – 49). Zr/Hf values of CC zircons similar range (43.4 – 53.6) over Ti-in-zircon temperatures that range from 689 – 858 °C. Zr/Hf values of OBA zircons fall into groups defined by the PPI and ER zircons.

Th/U values steeply co-vary with Yb/Dy values in all rhyolites, though some zircons from the ER show a shallow trend. Zr/Hf values of PFI zircons range from 38.4 – 48.8 at Ti-in-zircon crystallization temperatures between 682°C – 766°C. Like the PPI, ER zircons are split into two groups of low Zr/Hf (48.4 – 56.2) and high Zr/Hf (44 – 47).High Zr/Hf zircons in ER have somewhat elevated Th/U values. It is important to note that Zr/Hf values of ER zircons do not change predictably with Ti-in-zircon temperatures. Zr/Hf values in APR zircons also have little co-variation (45.5 – 50.6) with Ti-in-zircon temperatures (737°C – 898°C). Only the zircons that record the lowest Ti-in-zircon temperatures (701°C – 721°C) have distinctly lower Zr/Hf values.

Discussion

Resolution of U-Pb Age Populations – Episodes of Crystallization During Protracted Magma Evolution

Resolving the multimodal U-Pb spectra of the Chaxas Volcanic Complex is necessary for accurately describing the prominent periods of crystallization events throughout its history. Sufficient precision and large time differences between crystallization events may in some cases allow for straightforward discrimination between different subpopulations (Figure 2) that are readily interpreted as antecrystic zircon recycled from older intrusions. FAR, for instance, has two antecrystic populations at ca. 4.0 and 2.2 Ma that overlap that overlap with age spectra in older eruptions along with a young, autocrystic population at ca. 1.3 Ma (Figure 2). U-Pb crystallization ages from early Chaxas Complex and Pre-Chaxas eruptions do not show this fortuitous situation. Overdispersed U-Pb age spectra in all eruptions from APR to OBA show no clearly discernable subpopulations due to the large number of analyses with overlapping uncertainties (Figure 2). This is a common situation in LA-ICP-MS U-Pb geochronology that requires subjective inference to discriminate distinct subpopulations, or, statistical methodology that can resolve subpopulations from one another (e.g., Sambridge and Compston 1994).

Resolution between discrete populations in natural datasets is a common problem addressed in all fields, including U-Pb geochronology (Sambridge and Compston, 1994), that may be realized by mixture modeling techniques (McLachlan et al., 2019). The most common of these is Gaussian Mixture Modeling (GMM) which assumes that each underlying subpopulation is normally distributed. First attempts to resolve U-Pb subpopulations in zircon U-Pb ages presented in this study employed GMM modeling (Supplementary File 2). The model results were moderately successful but occasionally the resulting distributions were extremely sensitive to the variable uncertainties induced by dating methods with drastically different precisions used here, causing the estimated age of the subpopulation to be skewed from most of the data belonging to that subpopulation. In addition, crystallization events of zircon dictate that U-Pb age spectra are unlikely to be normally distributed due to a general decreasing crystallization rate with decreasing temperature (Harrison et al. 2007).

To generate mixture model results that are more representative of natural datasets, mixture modeling was thus performed using the Skew-Normal family as a density function (Prates et al., 2013), to which the normal distribution belongs (Azzalini, 2020).
Skew-Normal mixture modeling resulted in more effective identification of U-Pb age subpopulations that may be interpreted to represent the timing of major crystallization events in the magmatic system (Figure 5). Origins of antecrystic populations in successive eruptions are readily discernable by their overlap with those in progenitor eruptions. Autocrystic zircons formed during the last major crystallization event in each eruption also allows for a direct calculation of the continuous residence time of magma during the build-up to eruption (Δt), as defined by the difference between the weighted mean of the U-Pb zircon crystallization ages in the youngest subpopulation and the eruption age (**Table 1**). For the remainder of this contribution subpopulations are referred to as those identified through this method.

Pre-Chaxas Magmatic Evolution – Development of the Super-Sized Puripicar Magma Reservoir

Prolonged Early Construction of a Composite System Followed by Peak Magmatism

Protracted zircon age spectra are particularly useful for unveiling the construction and evolving architecture of large silicic systems (Cisneros de León et al., 2021). Resolved zircon subpopulations (Figure 5) in the Pre-Chaxas eruptions representing prolific crystallization events in the magmatic system support a protracted intrusion history and eventual accumulation of eruptible magma that are characteristic of large silicic systems (e.g., Kern et al., 2016). Prolonged t_{tot} of Pre-Chaxas zircons defined by variably diffuse and densely spaced zircon subpopulations connote a slowly constructed magmatic system that experienced heightened flux during the build-up to eruptive events within a few hundred thousand years of eruption, as defined by the Δt (Figure 2).

Early APVC magmatism underneath the Chaxas Volcanic Complex is documented by U-Pb subpopulations in the PPI at 8.7 Ma and 7.1 Ma, spanning back to the first and second major pulses of the APVC flare-up. Yet, eruption from the Chaxas Volcanic Complex magmatic system did not occur until the end of the second flare-up pulse with the APR at 5.44 Ma, followed more than one million years later by the 4.18 Ma PPI supereruption and the 3.73 Ma ER during the third pulse of the regional flare-up (Table 1). Early, infrequent intrusions into magmatic systems that saw peak magmatic activity millions of years later across the APVC have been previously attributed to peripheral intrusive activity relative to the loci of APVC volcanic activity (Kern et al. 2016) and the initial constructive phases of the Chaxas Volcanic Complex magmatic system was no different. Long-term construction of upper-crustal magmatic systems by episodic intrusion spanning millions of years has been documented in exposed crustal sections and has been inferred in volcano-plutonic systems globally (Coleman et al., 2004; Eddy et al., 2022; Karakas et al., 2019; Samperton et al., 2015), with transient high flux marking the prolific periods of magma accumulation, crustal growth, and volcanism in these systems. Spacing between zircon subpopulations in the Pre-Chaxas eruptions tracks this sequence well. Time differences between older subpopulations is on the order of 0.5 – 1.5 million years, whereas those subpopulations marking major crystallization events closer to eruption ages of the PPI and ER are more densely spaced, with differences of ≤ 200 thousand years. The weighted average ages of these subpopulations also permits prolonged Δts prior to major eruptions.

Based on the Δt of the PPI, final stages of continuous PPI magma accumulation occurred over approximately 500 thousand years. This extremely long time-domain of magma residence is consistent with the accumulation of voluminous silicic magma in the crust followed by up to one million years of residence time recorded in the APVC (Kaiser et al., 2017; Kern et al., 2016).

Crustal Assimilation Recorded in Zircon Zr/Hf Ratios

Decreasing Zr/Hf values in zircon is typically thought to represent chemical differentiation of zircon saturated melt by co-crystallization of zircon, allanite, xenotime, or garnet, whereas co-saturated titanite and rutile would act to increase Zr/Hf due to their relative partition coefficients (Bea et al., 2006; Claiborne et al., 2006). Key natural datasets exhibiting this systematic decrease are observed in the Bergell intrusion and the Spirit Mountain batholith that record extensive zircon crystallization (Claiborne et al., 2006; Samperton et al., 2015). However, a group of zircons hosted in the rhyolitic ER and APR, as well as the PPI have the highest Zr/Hf values of all those measured in this study (Figure 4). No clear trend ties high and low Zr/Hf zircons to one another that would indicate late saturation of zircon followed by extensive crystallization. Calculated Zr saturation temperatures (Boehnke et al., 2013) of PPI and ER glasses are also unremarkable and similar (Supplementary File 1), indicating zircon was probably continuously saturated during dacitic to rhyolitic melt production. These lines of evidence indicate that decreases in Zr/Hf ratios may not strictly reflect melt differentiation by crystallization of zircon or other Zr enriched phases. Comparison of Zr and Hf concentrations between whole rock (Zr/Hf: 29.8) and quenched anatectic melt (Zr/Hf: 41 - 47) of crustal xenoliths show that anatexis in the Andean crust will drastically increase the Zr/Hf ratio of contaminated melt (McLeod et al., 2012).

High Zr/Hf ratios of zircons in evolved melt of the Chaxas Volcanic Complex magmatic system may result from melting of fertile upper crustal lithologies. Zircon is well-known to be one of the first phases resorbed during anatexis (Miller et al., 2007) resulting in enriched Zr/Hf values of anatectic melt. Allanite stability also connotes it would quickly become unstable during melting (Engi, 2017). Moreover, rutile and especially titanite are well-known products of melting reactions (Zack and Kooijman, 2017), which would enhance preferential liberation of Zr over Hf into resident magma during assimilation. Whatever the exact melting sequence, the enriched Zr/Hf ratios of partially melted crustal xenoliths from the Andes relative to the refractory material (McLeod et al., 2012) supports the inference from trace element partitioning. To evaluate the feasibility of this model to explain the occurrence of high Zr/Hf ratios in evolved magmas at the

Chaxas Volcanic Complex, trace element modeling via fractional crystallization with linear varying partition coefficients (Greenland, 1970) along with fractional crystallization and assimilation (FCA) models (Cribb and Barton, 1996) was performed. These latter models differ from a classic assimilation and fractional crystallization model (DePaolo, 1981), as they account for the frequently observed observation that crystallization and assimilation operate at variable rates (Angeles-De La Torre et al. 2023). Model results indicate that ZTE can generally be explained by fractional crystallization of silicic melt (Figure 4). High Zr/Hf zircons, however, are best explained by the FCA model. Zircons in evolved Pre-Chaxas magmas show that assimilation of crustal material must be accounted for when interpreting trace element patterns in zircon with respect to Zr/Hf, and that high Zr/Hf zircon in rhyolites may signal an assimilation signature. These data are consistent with the high assimilation rates inferred for large magmatic systems constructed during high flux rates in the APVC.

Rhyolitic Melt Differentiation and Extraction

Two feldspar + quartz mineralogy of the ER and the other high-Si rhyolitic eruptions stratigraphically bracketing the PPI requires that the magmatic system also produced high-Si rhyolitic melt at low crustal pressures. Zircon petrochronologic data from the ER, PPI, and APR provide additional evidence of silicic melt extraction and differentiation in the upper crust, as frequently observed or inferred in exposed volcanic-plutonic systems (Schaen et al., 2021). Decreasing Th/U coupled to steepening REE patterns are associated with upper crustal melt evolution regardless of temperature, as experimental zircon compositions indicate that Th/U and Yb/Dy ratios do not change with decreasing temperature (Rubatto and Hermann, 2007). Variation in these ratios therefore results from co-saturation of REE enriched phases (e.g., apatite-britholite or allanite-chevkinite; Padilla and Gualda, 2016), or amphibole in the case of Yb/Dy. Fractionation models based on the mineralogy of the PPI and ER show that ZTE of constituent zircons can be explained by extensive fractionation of these magmas (Figure 4).

Melt extraction from granodioritic (dacitic) magma has been proposed as an efficient mechanism to produce high-silica melt in numerous volcanic and plutonic systems (Lewis et al., 2022; Schaen et al., 2021), largely as a result of latent heat buffering in large silicic systems (Lewis et al., 2022; Tavazzani et al. 2024). Production of these melts within a magmatic system that also produced one of the nine supereruptions on the APVC underscores the propensity for large magmatic systems to have a dynamic architecture that is not uniform throughout its vertical extent nor across time. The La Pacana Caldera Complex that produced the Toconao rhyolite overlain by the Atana dacite in the APVC (Lindsay et al., 2001) underscores this point. Despite their stratigraphic relationships, the Toconao ignimbrite carries older zircon crystals than the Atana ignimbrite, indicating that the Toconao rhyolitic magma saturated in zircon ca. 500 kyr prior to the parental Atana dacitic magma (Schmitt et al., 2003).. Melt extraction of rhyolitic magma within large systems throughout the APVC supports that this is an efficient and fundamental process for rhyolite production (Tavazzani et al., 2024), as similarly observed here in the Chaxas Volcanic Complex.

The Chaxas Complex – Small Scale Distributed Upper Crustal Magmatism During Waning Magmatic Flux

Decreasing Upper Crustal Thermal Events and Crystal Accumulation Recorded in Zircon

Loss of overdispersion in zircon age spectra and the overall decrease of t_{tot} and Δt in the Chaxas Complex eruptions from PFI through YBA (Figure 2) indicate that frequency of crystallization events induced by magmatic intrusion into the upper crustal magmatic system decreased over time. Zircon subpopulations are less diffuse compared to those of the Pre-Chaxas formation (Figure 5) and connote shorter residence times, as seen most directly in the decrease of t_{tot} and Δt. Chaxas Complex zircon subpopulations complement zircon records which show tightly distributed spectra are induced by sporadic recharge events during waning flux (Friedrichs et al., 2021) as opposed to some magmatic systems that suggest high frequency of recharge events late in the correspondent magmatic lifecycles (Farina et al., 2024; Friedrichs et al., 2021). This is consistent with the regional diminution of magmatic flux into the upper crust recorded after the peak of the APVC flare-up ~4 Ma (Kern et al., 2016; Bertin 2023).

ZTE of Chaxas Complex eruptions provide additional evidence for the isolation of ephemeral magma batches late in its history. Little variation is present in the Zr/Hf ratios of these zircons, and other trace element trends (i.e., lower U, limited REE pattern variance) suggest less variation in host melt composition (Figure 4). Invariance of these ratios are inconsistent with repeated saturation-dissolution of co-crystallizing phases observed in volcanic systems of relatively vigorous magmatic activity (Dechert et al., 2024), or high assimilation rates, as described above for the Pre-Chaxas stage. Crystallization temperatures estimated from Ti concentrations in zircon are also dominantly cooler in Chaxas Complex eruptions although a few temperature estimates are high (Figure 3) consistent with less vigorous homogenization during sporadic recharge. Overall ZTE in these eruptions are interpreted to represent near spatially uniform zircon crystallization throughout a remnant or small volume upper crustal magma batch that experienced only subtle geochemical and thermal variations during heating events.

Zircon age spectra of the Chaxas Volcanic Complex eruptions have subpopulations that overlap with older generations of zircons in prior eruptions (Figure 2, Figure 5), or in the case of PPI record initial intrusion histories. Zircon subpopulations formed hundreds of thousands to millions of years before the eruptive event that carried them to the surface (Figure 5) indicate that near-solidus to sub-solidus plutonic material crystallized from older or progenitor magma batches was being recycled into erupted products. Recycling of this plutonic material is a critical observation as this indicates that 1) recharging magmatic intrusions were focused into older pathways, consistent with plutonic observations suggesting this is common (Memeti et al., 2021) and 2) crystals from previous magmatic episodes contributes to erupted material during silicic eruptions via cannibalization or recycling (Angeles-De La Torre et al., 2023; Bacon and Lowenstern, 2005).

Multiple generations of zircon subpopulations make it evident that long-lived silicic magmatic systems experience repeated intrusion through old magmatic pathways. This phenomenon is well-known and geochronologically recorded at the crystal scale (Bacon and Lowenstern 2005) and geologically and geochemically inferred at the regional scale (Lipman et al., 1978). The volcanic record at the Chaxas Complex records the construction and evolution of a large silicic plutonic complex through the final stages of its lifecycle.

The change from crystal cargo recording diverse crystallization conditions over long durations seen in Pre-Chaxas rocks to simpler crystal cargo formed over shorter durations in the Chaxas Complex signals a change from a growing (waxing), composite magma reservoir to one that was cooler (waning) and could only sustain small, internally homogenous but distinct batches of magma. This implies that voluminous silicic mushy remnants of the Pre-Chaxas reservoir began cooling to form subvolcanic plutons (e.g., Lipman and Bachmann 2015) that were cross-cut and intruded by later silicic magmas. Efficient cannibalization of plutonic material diminished due to final solidification of voluminous magmatic intrusions emplaced during the Pre-Chaxas era, as recorded by loss of the characteristically diverse zircon cargo otherwise seen in Pre-Chaxas eruptions. The antecrystic subpopulations, interpreted to represent the cumulates left over largely from the Pre-Chaxas era of high flux magmatism. Formation of silicic cumulates by *in-situ* differentiation and sporadic thermal rejuvenation is a critical process by which upper crustal magma reservoirs are fossilized as silicic plutons (Eddy et al., 2022) and the Chaxas Volcanic Complex appears to be a superb volcanic archive that also records the influence of magmatic flux.

Varying Thermal Flux in an Architecturally Evolving System

To quantify the fluxes during the lifecycle of the Chaxas Volcanic Complex, synthetic zircon distributions were modeled using the "MagmaThermoKinematics" code (Supplementary File 2) to create synthetic zircon distributions, the structures of which are sensitive to timing of cooling events and therefore magmatic flux (Schmitt et al., 2023). The best estimate for the average flux during the 2.5 million years leading up to the eruption of the PPI ignimbrite (Figure 6) are 0.002 km^3/yr, with the flux leading up to eruption reaching 0.005 km^3/yr and a total volume of 5321 km^3 (Table 2). This estimate is a minimum because the melt present time for the PPI was approximately 500 thousand years based on the calculated Δt and model runs were restricted to 2.5 million years for computational purposes. Thermal models for the Chaxas Complex stage using zircon U-Pb crystallization ages from the MBA eruption were also performed. Flux during the significantly diminished volcanic activity of the Chaxas Complex is estimated to average 7×10^{-4} km^3/yr (Figure 6). This flux estimate is a minimum, because the modeled synthetic zircon distribution used to derive a flux estimate for the MBA (Figure 6) is compared to a set of zircon ages with even dispersion representing a single crystallization event. Overall, significantly lower thermal fluxes are recorded in the zircon spectra of the Chaxas Complex eruptions compared with those returned for the Pre-Chaxas stage represented by the PPI zircon ages. This difference in the fluxes is consistent with inferences about the regional APVC wide flux by previous works (de Silva and Gosnold, 2007; Kern et al., 2016).

Flux estimates for the Pre-Chaxas stage are on the exact order of magnitude estimated for the formation of large upper crustal reservoirs that birth voluminous eruptions (Gelman et al., 2013) and slightly higher than the late Pleistocene lava domes in the APVC that were extracted from what appears to be a contiguous upper crustal reservoir that failed to produce a supereruption (Tierney et al., 2016). Compared to flux estimates for the region that rely on assumptions of volcanic to plutonic ratios (Bertin et al., 2023; de Silva and Gosnold, 2007), the flux estimates made here are either the same or approximately one order of magnitude lower. Higher flux estimates of 0.012 – 0.06 km^3/yr (de Silva and Gosnold, 2007) are attributed to integrating the volumes over short periods of pulses on the order of a few hundred thousand years. More recent modeling efforts (Bertin et al., 2023) found intrusive flux rates for the region to average 0.00048 km^3/yr for a 23 km section of arc like the Chaxas Volcanic Complex, and up to 0.012 km^3/yr for the highest instantaneous flux estimates. Differences for the region can ultimately be attributed to assumptions about the time domain over which the volumes are integrated, and ultimately all of these assumptions still put the flux estimates for the Pre-Chaxas reservoir well above the 20 km^3 / one km of arc / one million year flux estimate that is considered the baseline for magmatic flare-ups (Jicha and Jagoutz, 2015).

The flux and the thermal history of the Chaxas Complex as modelled for the MBA eruption is an order of magnitude lower than the Pre-Chaxas (PPI) state of the magmatic system. The maximum estimate of 7×10^{-4} km^3/yr we have derived is typical of steady state (long term secular background) fluxes estimated for volcanic arcs (Bertin et al., 2023; Jicha and Jagoutz, 2015) (Table 2). This is consistent with the Chaxas Complex being constructed under the post-flare-up, waning flux regime of the APVC.

Time-Resolved Architectural Changes through Zircon Petrochronology

One key observation in the petrochronologic dataset gathered here is the relationship between zircon age, chemistry, and crystallization temperature (Figure 7, Figure 8). Pre-Chaxas eruptions hosted zircons that show a general decrease in Eu/Eu* over time, indicating that the reservoir produced increasingly evolved magmas as it grew and assimilated crustal, as shown in partitioning models (Figure 4). Despite this evolution and the physical mixing between magmas spanning a large compositional range in the Pre-Chaxas system, lack of a concomitant temperature trend in the zircons suggests efficient temperature cycling via advection into the upper crust and buffering by the presence of a large silicic system of broadly dacitic composition. Conversely, the Chaxas Complex zircon crystal cargo show clear evidence of recycling through temperature-age-chemistry relationships. Younger zircon crystal cargo have similar, intermediate Eu/Eu* values and less ZTE variability, as described above, which attests to less interaction between compositionally diverse melts than during the Pre-Chaxas stage. Recycled crystal cargo in the Chaxas Complex eruptions contrast with the autocrystic zircon, as the recycled zircon has a large range of chemical variability and are lower in crystallization temperature (Figure 8). Combined age-temperature-chemistry relationships of recycled crystals shows that these zircons were cannibalized from Pre-Chaxas or earlier Chaxas Complex magmatic remnants that were either held at near-solidus temperatures or recycled from associated plutonic material. Given that thermal models, field observations, and natural datasets dictate magmatic reservoirs are unlikely to remain melt rich for more than 1 million years at a maximum (Annen, 2009; Kaiser et al., 2017), recycled zircons with low crystallization temperatures are interpreted as crystals disaggregated from consanguineous plutonic progenitors.

Zircon petrochronology of the Chaxas Complex (Figure 7) does not uniquely support that either upper crustal magma was stored entirely in near- to sub-solidus conditions (Cooper, 2019) or in a dominantly melt present state (Barboni et al., 2016). Rather, the zircon record in the Chaxas Volcanic Complex suggests that the architecture of the reservoir was dynamic and the organization and characteristic lifecycle of melt-dominated magma changed over time. Mixed geochemical-age populations of zircon indicates that at any given time during the evolution of the Chaxas reservoir, both solidified plutonic material and melt rich lenses (Figure 8) coexisted and were available for sampling during eruption.

Probing the Remnant Composite Plutonic System Beneath the Chaxas Volcanic Complex

Flux estimates for Pre-Chaxas eruptions are lower than the extensive Southern Rocky Mountain Volcanic Field (SRMVF) that has an estimated flux of 0.05 km^3/yr (Lipman and Bachmann, 2015) and contains numerous caldera complexes underpinned by batholiths with volumes on the order of 10^3 km^3. The flux and volume estimate from the PPI is expectedly smaller than more voluminous flare-ups such as the SRMVF (Best et al., 2016). Rather, the Pre-Chaxas flux estimates (avg.: 2 x 10^{-3} km^3/yr) and volume (~5300 km^3) are directly comparable to the 3.5 x 10^{-3} km^3/yr flux and 1200 – 9000 km^3 volume estimated for the long-lived and voluminous Mt. Stuart pluton (Lipman and Bachmann, 2015; Matzel et al., 2006) (Table 2). Interestingly, the best-fit intrusive history for the Pre-Chaxas magmatic history that accounts for the variable slope in the empirical cumulative distribution of the observed U-Pb crystallization ages of the PPI (Figure 6) is characterized by pulses of high flux separated by lower flux conditions, similar to that observed at the Mt. Stuart pluton. Sharp geochronological discontinuities across otherwise compositionally homogenous silicic domains within Mt. Stuart also attest to its incremental, upper crustal history. As an intrusive proxy to the volcanic Chaxas Volcanic Complex, the similar magmatic history and characteristics observed at the Mt. Stuart batholith indicates that the large and long-lived volcanic system that produced the PPI is now underpinned by a similar composite, silicic plutonic complex. As regional flux waned, however, the intrusive volume into the upper crust drastically diminished to a maximum of 100's of km^3 at a single period and likely less based on this estimate being an upper bound for the MBA (Figure 6). Using the 300 km^3 estimated intrusion history across the time domain of the MBA zircons (460 kyr), no more than 1500 km^3 of magma was emplaced during the entire Pre-Chaxas stage. As supported by the ZTE and age spectra of the Chaxas Complex eruptions, the resident melt during the latter stages of the Chaxas Volcanic Complex was likely short and emplaced into a voluminous silicic mush that had largely solidified following catastrophic eruption and peak magmatic activity (Figure 8).

Conclusions

Magmatic evolution of the Chaxas Volcanic Complex system captures a transition from large-volume, integrative magmatism during the Pre-Chaxas stage (5.4 – 4.18 Ma) to lower-volume, discrete magmatism during the Chaxas Complex phase (3.54 – 1.34 Ma) that parallels the inferred thermal history of the Altiplano-Puna Volcanic Complex ignimbrite flare-up. The Pre-Chaxas stage coincides with the peak of the flare-up and climaxed with the 4.18 Ma Puripicar supereruption that evacuated magma with zircons that display an overdispersed zircon age spectrum with compositionally variable zircon populations. These features reflect elevated magmatic fluxes (minimum 5×10^{-3} km^3/yr) and prolific cannibalization of fossilized progenitor intrusions culminating with the ≥ 500 km^3 Puripicar supereruption. During this period, prolific crustal assimilation is recorded by high Zr/Hf ratios in zircon reflecting growth in melts from anatexis of fertile crust. In contrast, the subsequent Chaxas Complex reflects a waning magmatic system, with lower fluxes (maximum $<7 \times 10^{-4}$ km^3/yr) accounting for simpler zircon age populations, less variable zircon trace elements, that connote smaller, discrete magma bodies evolving within a long-lived crystal mush. The persistent presence of antecrysts emphasizes the thermal and physical continuity between eruptive episodes. The prolonged magmatic history at the Chaxas Volcanic Complex demonstrates that simplified magmatic architectures and storage conditions are not likely to be characteristic across the entire lifecycle of a magmatic system. Instead, the system records multi-scale, temporally complex processes contributing to the construction and eventual solidification of a long-lived silicic magmatic locus, which we estimate to have built a > 5500 km^3 composite granodioritic pluton underneath the present day Chaxas Complex.

Acknowledgements

CTL is indebted to the Geological Society of America, the Sharp family, the Mazamas mountaineering organization, and the Central Oregon Geoscience Society for their various funding initiatives that made this work possible. CTL is supported through a Graduate Research Assistantship where he works in the W.M. Keck Collaboratory at Oregon State University. This work was not possible without the encouragement and comradery of Chris Russo and Adam Kent. We are grateful for Christian Metzke of Alma Gaucho Expeditions, Matias Villaroel, and Alex Cisneros who helped us in the field. Logistical support and sample export from Chile was enabled by Felipe Aguilera (Universidad del Norte) and Benigno Godoy (Universidad de Chile). Axel Schmitt provided insightful comment on an earlier version of this manuscript.

References

Angeles-De La Torre, C.A., Schmitt, A.K., Lovera, O.M., Gassert, H., Gerdes, A., Harvey, J.C., 2023. A common magma source for plutonic and volcanic rocks of The Geysers geothermal field, California: Volume and intrusive history derived from zircon. Chemical Geology 624, 121414. https://doi.org/10.1016/j.chemgeo.2023.121414

Annen, C., 2009. From plutons to magma chambers: Thermal constraints on the accumulation of eruptible silicic magma in the upper crust. Earth and Planetary Science Letters 284, 409–416. https://doi.org/10.1016/j.epsl.2009.05.006

Azzalini, A., 2020. FURTHER RESULTS ON A CLASS OF DISTRIBUTIONS WHICH INCLUDES THE NORMAL ONES. Statistica 2.

Bacon, C., Lowenstern, J., 2005. Late Pleistocene granodiorite source for recycled zircon and phenocrysts in rhyodacite lava at Crater Lake, Oregon. Earth and Planetary Science Letters 233, 277–293. https://doi.org/10.1016/j.epsl.2005.02.012

Barboni, M., Boehnke, P., Schmitt, A.K., Mark Harrison, T., Shane, P., Bouvier, A.S., Baumgartner, L., 2016. Warm storage for arc magmas. Proceedings of the National Academy of Sciences of the United States of America 113, 13959–13964. https://doi.org/10.1073/pnas.1616129113

Bea, F., Montero, P., Ortega, M., 2006. A LA-ICP-MS EVALUATION OF Zr RESERVOIRS IN COMMON CRUSTAL ROCKS: IMPLICATIONS FOR Zr AND Hf GEOCHEMISTRY, AND ZIRCON-FORMING PROCESSES. The Canadian Mineralogist 44, 693–714. https://doi.org/10.2113/gscanmin.44.3.693

Bertin, D., De Silva, S.L., Lindsay, J.M., Cronin, S.J., Caffe, P.J., Connor, C.B., Grosse, P., Báez, W., Bustos, E., Constantinescu, R., 2023. Magmatic addition rates differentiate periods of steady-state versus flare-up magmatism in the Central Andean arc. Commun Earth Environ 4, 75. https://doi.org/10.1038/s43247-023-00744-2

Best, M.G., Christiansen, E.H., de Silva, S., Lipman, P.W., 2016. Slab-rollback ignimbrite flareups in the southern Great Basin and other Cenozoic American arcs: A distinct style of arc volcanism. Geosphere 12, 1097–1135. https://doi.org/10.1130/GES01285.1

Boehnke, P., Watson, E.B., Trail, D., Harrison, T.M., Schmitt, A.K., 2013. Zircon saturation re-revisited. Chemical Geology 351, 324–334. https://doi.org/10.1016/j.chemgeo.2013.05.028

Burns, D.H., de Silva, S.L., 2023. Andesites and evolution of the continental crust: Perspectives from the Central Volcanic Zone of the Andes. Front. Earth Sci. 10, 961130. https://doi.org/10.3389/feart.2022.961130

Cisneros de León, A., Schmitt, A.K., Kutterolf, S., Schindlbeck-Belo, J.C., Hernández, W., Sims, K.W.W., Garrison, J., Kant, L.B., Weber, B., Wang, K. -L., Lee, H. -Y., Trumbull, R.B., 2021. Zircon and Melt Extraction From a Long-Lived and Vertically Extensive Magma System Underneath Ilopango Caldera (El Salvador). Geochem Geophys Geosyst 22. https://doi.org/10.1029/2020GC009507

Claiborne, L., Miller, C.F., Walker, B.A., Wooden, J.L., Mazdab, F.K., Bea, F., 2006. Tracking magmatic processes through Zr/Hf ratios in rocks and Hf and Ti zoning in zircons: An example from the Spirit Mountain batholith, Nevada. Mineral. mag. 70, 517–543. https://doi.org/10.1180/0026461067050348

Coleman, D.S., Gray, W., Glazner, A.F., 2004. Rethinking the emplacement and evolution of zoned plutons: Geochronologic evidence for incremental assembly of the Tuolumne Intrusive Suite, California. Geology 32, 433–436. https://doi.org/10.1130/G20220.1

Coney, P.J., Reynolds, S.J., 1977. Cordilleran Benioff zones. Nature 270, 403–406. https://doi.org/10.1038/270403a0

Cooper, K.M., 2019. Time scales and temperatures of crystal storage in magma reservoirs: implications for magma reservoir dynamics. Phil. Trans. R. Soc. A. 377, 20180009. https://doi.org/10.1098/rsta.2018.0009

Cribb, J.W., Barton, M., 1996. Geochemical effects of decoupled fractional crystallization and crustal assimilation. Lithos 37, 293–307. https://doi.org/10.1016/0024-4937(95)00027-5

de Silva, S., Kay, S.M., 2018. Turning up the heat: High-flux magmatism in the central andes. Elements 14, 245–250. https://doi.org/10.2138/gselements.14.4.245

de Silva, S.L., 1989. Geochronology and stratigraphy of the ignimbrites from the 21 ° 30' S to 23 ° 30' S portion of the Central Andes of Northern Chile.

de Silva, S.L., Gosnold, W.D., 2007. Episodic construction of batholiths: Insights from the spatiotemporal development of an ignimbrite flare-up. Journal of Volcanology and Geothermal Research 167, 320–335. https://doi.org/10.1016/j.jvolgeores.2007.07.015

Dechert, A.E., Andersen, N.L., Dufek, J., Jilly, C.E., 2024. Zircon Constraints on the Eruptive Sequence and Magma Evolution of Rhyolites at South Sister Volcano, Oregon. Geochem Geophys Geosyst 25, e2024GC011680. https://doi.org/10.1029/2024GC011680

DePaolo, D.J., 1981. Trace element and isotopc effects of combined wallrock assimilation and fractional crystallization. Earth and Planetary Science Letters 53, 189–202.

Eddy, M.P., Pamukçu, A., Schoene, B., Steiner-Leach, T., Bell, E.A., 2022. Constraints on the timescales and processes that led to high-SiO2 rhyolite production in the Searchlight pluton, Nevada, USA. Geosphere 18, 1000–1019. https://doi.org/10.1130/GES02439.1

Engi, M., 2017. Petrochronology Based on REE-Minerals: Monazite, Allanite, Xenotime, Apatite. Reviews in Mineralogy and Geochemistry 83, 365–418. https://doi.org/10.2138/rmg.2017.83.12

Farina, F., Weber, G., Hartung, E., Rubatto, D., Forni, F., Luisier, C., Caricchi, L., 2024. Magma flux variations triggering shallow-level emplacement of the Takidani pluton (Japan): Insights into the volcanic-plutonic connection. Earth and Planetary Science Letters 635, 118688. https://doi.org/10.1016/j.epsl.2024.118688

Ferry, J.M., Watson, E.B., 2007. New thermodynamic models and revised calibrations for the Ti-in-zircon and Zr-in-rutile thermometers. Contrib Mineral Petrol 154, 429–437. https://doi.org/10.1007/s00410-007-0201-0

Friedrichs, B., Schmitt, A.K., Lovera, O.M., Atıcı, G., 2021. Zircon as a recorder of contrasting magma recharge and eruptive recurrence patterns. Earth and Planetary Science Letters 571, 117104. https://doi.org/10.1016/j.epsl.2021.117104

Gelman, S.E., Gutiérrez, F.J., Bachmann, O., 2013. On the longevity of large upper crustal silicic magma reservoirs. Geology 41, 759–762. https://doi.org/10.1130/G34241.1

Grant, M.L., Wilde, S.A., Wu, F., Yang, J., 2009. The application of zircon cathodoluminescence imaging, Th–U–Pb chemistry and U–Pb ages in interpreting discrete magmatic and high-grade metamorphic events in the North China Craton at the Archean/Proterozoic boundary. Chemical Geology 261, 155–171. https://doi.org/10.1016/j.chemgeo.2008.11.002

Greenland, L.P., 1970. An equation for trace element distribution during magmatic crystallization. The American Mineralogist 55, 455–465.

Grocke, S.B., Andrews, B.J., de Silva, S.L., 2017. Experimental and petrological constraints on long-term magma dynamics and post-climactic eruptions at the Cerro Galán caldera system, NW Argentina. Journal of Volcanology and Geothermal Research 347, 296–311. https://doi.org/10.1016/j.jvolgeores.2017.09.021

Harrison, T.M., Watson, E.B., Aikman, A.B., 2007. Temperature spectra of zircon crystallization in plutonic rocks. Geol 35, 635. https://doi.org/10.1130/G23505A.1

Horstwood, M.S.A., Košler, J., Gehrels, G., Jackson, S.E., McLean, N.M., Paton, C., Pearson, N.J., Sircombe, K., Sylvester, P., Vermeesch, P., Bowring, J.F., Condon, D.J., Schoene, B., 2016. Community-Derived Standards for LA - ICP - MS U-(Th-)Pb Geochronology – Uncertainty Propagation, Age Interpretation and Data Reporting. Geostand Geoanal Res 40, 311–332. https://doi.org/10.1111/j.1751-908X.2016.00379.x

Jicha, B.R., Jagoutz, O., 2015. Magma Production Rates for Intraoceanic Arcs. Elements 11, 105–111. https://doi.org/10.2113/gselements.11.2.105

Kaiser, J.F., de Silva, S., Schmitt, A.K., Economos, R., Sunagua, M., 2017. Million-year melt–presence in monotonous intermediate magma for a volcanic–plutonic assemblage in the Central Andes: Contrasting histories of crystal-rich and crystal-poor super-sized silicic magmas. Earth and Planetary Science Letters 457, 73–86. https://doi.org/10.1016/j.epsl.2016.09.048

Karakas, O., Wotzlaw, J.-F., Guillong, M., Ulmer, P., Brack, P., Economos, R., Bergantz, G.W., Sinigoi, S., Bachmann, O., 2019. The pace of crustal-scale magma accretion and differentiation beneath silicic caldera volcanoes. Geology 47, 719–723. https://doi.org/10.1130/G46020.1

Kay, S.M., Coira, B.L., Caffe, P.J., Chen, C.H., 2010. Regional chemical diversity, crustal and mantle sources and evolution of central Andean Puna plateau ignimbrites. Journal of Volcanology and Geothermal Research 198, 81–111. https://doi.org/10.1016/j.jvolgeores.2010.08.013

Kern, J.M., de Silva, S.L., Schmitt, A.K., Kaiser, J.F., Iriarte, A.R., Economos, R., 2016. Geochronological imaging of an episodically constructed subvolcanic batholith: U-Pb in zircon chronochemistry of the Altiplano-Puna Volcanic Complex of the Central Andes. Geosphere 12, 1054–1077. https://doi.org/10.1130/GES01258.1

Lewis, C., de Silva, S., Cisneros De Leon, A., Burns, D., Villarroel, M., 2025. Effusive volcanic microcosm of a regional ignimbrite flare-up: Prolonged life cycle of the Chaxas Complex, northern Chile, and its influence on modern volcanic arc character. Geological Society of America Bulletin. https://doi.org/10.1130/B37909.1

Lewis, C.T., de Silva, S.L., Burns, D.H., 2022. Rhyolitic melt production in the midst of a continental arc flare-up—The heterogeneous Caspana ignimbrite of the Altiplano-Puna volcanic complex of the Central Andes. Geosphere 18, 1679–1709. https://doi.org/10.1130/GES02462.1

Lipman, P.W., Bachmann, O., 2015. Ignimbrites to batholiths: Integrating perspectives from geological, geophysical, and geochronological data. Geosphere 11, 705–743. https://doi.org/10.1130/GES01091.1

Lipman, P.W., Doe, B.R., Hedge, C.E., Steven, T.A., 1978. Petrologic evolution of the San Juan volcanic field, southwestern Colorado: Pb and Sr isotope evidence. Geol Soc America Bull 89, 59. https://doi.org/10.1130/0016-7606(1978)89<59:PEOTSJ>2.0.CO;2

Lubbers, J., Kent, A.J.R., Russo, C., 2025. lasertram: A Python library for time resolved analysis of laser ablation inductively coupled plasma mass spectrometry data. Applied Computing and Geosciences 100225. https://doi.org/10.1016/j.acags.2025.100225

Matzel, J.E.P., Bowring, S.A., Miller, R.B., 2006. Time scales of pluton construction at differing crustal levels: Examples from the Mount Stuart and Tenpeak intrusions, North Cascades, Washington. Geological Society of America Bulletin 118, 1412–1430. https://doi.org/10.1130/B25923.1

McLachlan, G.J., Lee, S.X., Rathnayake, S.I., 2019. Finite Mixture Models.

McLeod, C.L., Davidson, J.P., Nowell, G.M., de Silva, S.L., 2012. Disequilibrium melting during crustal anatexis and implications for modeling open magmatic systems. Geology 40, 435–438. https://doi.org/10.1130/G33000.1

Memeti, V., Paterson, S.R., Mundil, R., 2021. Coupled magmatic and host rock processes during the initiation of the Tuolumne Intrusive Complex, Sierra Nevada, California, USA: A transition from ephemeral sheets to long-lived, active magma mushes. GSA Bulletin 1–28. https://doi.org/10.1130/b35871.1

Miller, J.S., Matzel, J.E.P., Miller, C.F., Burgess, S.D., Miller, R.B., 2007. Zircon growth and recycling during the assembly of large, composite arc plutons. Journal of Volcanology and Geothermal Research 167, 282–299. https://doi.org/10.1016/j.jvolgeores.2007.04.019

National Academies of Sciences, Engineering, and Medicine, 2017. Volcanic eruptions and their repose, unrest, precursors, and timing, Volcanic Eruptions and Their Repose, Unrest, Precursors, and Timing. https://doi.org/10.17226/24650

Padilla, A.J., Gualda, G.A.R., 2016. Crystal-melt elemental partitioning in silicic magmatic systems: An example from the Peach Spring Tuff high-silica rhyolite, Southwest USA. Chemical Geology 440, 326–344. https://doi.org/10.1016/j.chemgeo.2016.07.004

Paterson, S.R., Okaya, D., Memeti, V., Economos, R., Miller, R.B., 2011. Magma addition and flux calculations of incrementally constructed magma chambers in continental margin arcs: Combined field, geochronologic, and thermal modeling studies. Geosphere 7, 1439–1468. https://doi.org/10.1130/GES00696.1

Prates, M.O., Cabral, C.R.B., Lachos, V.H., 2013. mixsmsn: Fitting Finite Mixture of Scale Mixture of Skew-Normal Distributions. Journal of Statistical Software 54.

Pritchard, M.E., de Silva, S.L., Michelfelder, G., Zandt, G., McNutt, S.R., Gottsmann, J., West, M.E., Blundy, J., Christensen, D.H., Finnegan, N.J., Minaya, E., Sparks, R.S.J., Sunagua, M., Unsworth, M.J., Alvizuri, C., Comeau, M.J., del Potro, R., Díaz, D., Diez, M., Farrell, A., Henderson, S.T., Jay, J.A., Lopez, T., Legrand, D., Naranjo, J.A., McFarlin, H., Muir, D., Perkins, J.P., Spica, Z., Wilder, A., Ward, K.M., 2018. Synthesis: PLUTONS: Investigating the relationship between pluton growth and volcanism in the Central Andes. Geosphere 14, 954–982. https://doi.org/10.1130/GES01578.1

Rubatto, D., Hermann, J., 2007. Experimental zircon/melt and zircon/garnet trace element partitioning and implications for the geochronology of crustal rocks. Chemical Geology 241, 38–61. https://doi.org/10.1016/j.chemgeo.2007.01.027

Salisbury, M.J., Jicha, B.R., de Silva, S.L., Singer, B.S., Jiménez, N.C., Ort, M.H., 2011. 40Ar/39Ar chronostratigraphy of Altiplano-Puna volcanic complex ignimbrites reveals the development of a major magmatic province. Bulletin of the Geological Society of America 123, 821–840. https://doi.org/10.1130/B30280.1

Sambridge, M.S., Compston, W., 1994. Mixture modeling of multi-component data sets with application to ion-probe zircon ages. Earth and Planetary Science Letters 128, 373–390. https://doi.org/10.1016/0012-821X(94)90157-0

Samperton, K.M., Bell, E.A., Barboni, M., Keller, C.B., Schoene, B., 2017. Zircon age-temperature-compositional spectra in plutonic rocks. Geology 45, 983–986. https://doi.org/10.1130/G38645.1

Samperton, K.M., Schoene, B., Cottle, J.M., Brenhin Keller, C., Crowley, J.L., Schmitz, M.D., 2015. Magma emplacement, differentiation and cooling in the middle crust: Integrated zircon geochronological–geochemical constraints from the Bergell Intrusion, Central Alps. Chemical Geology 417, 322–340. https://doi.org/10.1016/j.chemgeo.2015.10.024

Schaen, A.J., Schoene, B., Dufek, J., Singer, B.S., Eddy, M.P., Jicha, B.R., Cottle, J.M., 2021. Transient rhyolite melt extraction to produce a shallow granitic pluton. Sci. Adv. 7, eabf0604. https://doi.org/10.1126/sciadv.abf0604

Schmitt, A.K., Lindsay, J.M., De Silva, S., Trumbull, R.B., 2003. U-Pb zircon chronostratigraphy of early-Pliocene ignimbrites from La Pacana, north Chile: Implications for the formation of stratified magma chambers. Journal of Volcanology and Geothermal Research 120, 43–53. https://doi.org/10.1016/S0377-0273(02)00359-1

Schmitt, A.K., Sliwinski, J., Caricchi, L., Bachmann, O., Riel, N., Kaus, B.J.P., Cisneros De Léon, A., Cornet, J., Friedrichs, B., Lovera, O., Sheldrake, T., Weber, G., 2023. Zircon age spectra to quantify magma evolution. Geosphere 19, 1006–1031. https://doi.org/10.1130/GES02563.1

Schmitt, A.K., Stockli, D.F., Lindsay, J.M., Robertson, R., Lovera, O.M., Kislitsyn, R., 2010. Episodic growth and homogenization of plutonic roots in arc volcanoes from combined U–Th and (U–Th)/He zircon dating. Earth and Planetary Science Letters 295, 91–103. https://doi.org/10.1016/j.epsl.2010.03.028

Schmitt, A.K., Vazquez, J.A., 2017. Secondary Ionization Mass Spectrometry Analysis in Petrochronology. Reviews in Mineralogy and Geochemistry 83, 199–230. https://doi.org/10.2138/rmg.2017.83.7

Tavazzani, L., Economos, R.C., Peres, S., Demarchi, G., Sinigoi, S., Bachmann, O., 2024. The Role of Latent Heat Buffering in the Generation of High-Silica Rhyolites. Journal of Petrology 65, egae072. https://doi.org/10.1093/petrology/egae072

Tavazzani, L., Wotzlaw, J.-F., Economos, R., Sinigoi, S., Demarchi, G., Szymanowski, D., Laurent, O., Bachmann, O., Chelle-Michou, C., 2023. High-precision zircon age spectra record the dynamics and evolution of large open-system silicic magma reservoirs. Earth and Planetary Science Letters 623, 118432. https://doi.org/10.1016/j.epsl.2023.118432

Tierney, C.R., Schmitt, A.K., Lovera, O.M., de Silva, S.L., 2016. Voluminous plutonism during volcanic quiescence revealed by thermochemical modeling of zircon. Geology 44, 683–686. https://doi.org/10.1130/G37968.1

Vazquez, J.A., Reid, M.R., 2004. Probing the Accumulation History of the Voluminous Toba Magma. Science 305, 991–994. https://doi.org/10.1126/science.1096994

Ward, K.M., Zandt, G., Beck, S.L., Christensen, D.H., McFarlin, H., 2014. Seismic imaging of the magmatic underpinnings beneath the Altiplano-Puna volcanic complex from the joint inversion of surface wave dispersion and receiver functions. Earth and Planetary Science Letters 404, 43–53. https://doi.org/10.1016/j.epsl.2014.07.022

Zack, T., Kooijman, E., 2017. Petrology and Geochronology of Rutile. Reviews in Mineralogy and Geochemistry 83, 443–467. https://doi.org/10.2138/rmg.2017.83.14

Tables

Table 1: Generalized Stratigraphy of Chaxas Volcanic Complex

Formation	Unit	Unit Abbreviaton	Eruption Age (Ma)	Eruption Type	t_{tot}	Δt
Chaxas Complex	Final del Agua Rhyolite	FAR	1.24 ± 0.05	PDC	0	0.2
	Youngest B&A	YBA	1.834 ± 0.00085	B&A	2.5	0.09
	Cerro Chaxas	CC	1.86 ± 0.056	Dome	1	0.15
	Middle B&A	MBA	2.35 ± 0.01	B&A	0.5	0.1
	Oldest B&A	OBA	2.75 ± 0.19	B&A	2.2	0.04
	Pyroclastic Fallout I	PF I	3.54 ± 0.33	PF	2.3	0.19
Pre-Chaxas	Embaucador Rhyolite	ER	3.73 ± 0.02	PDC	3.5	0.23
	Puripicar Ignimbrite	PPI	4.18 ± 0.03	PDC	4.4	0.52
	Agua Perdida Rhyolite	APR	5.44 ± 0.01	PDC	1.3	0.13

ttot and Δt in units of Myr, as defined in the text

Table 2: Estimated Magmatic Flux for the Chaxas-Puripicar System and Other Notable Magmatic Systems

	High Flux Regime (PPI)	Low Flux Regime (CC)	SRMVF	Mount Stuart Pluton
Avg. Flux	0.0021	0.0007	0.05	0.0035
Min Instantaneous Flux	0.0003	0.0004		
Max Instantaneous Flux	0.0052	0.0013		

Flux estimates for SRMVF (Lipman, 2007; Farmer et al., 2008) and Mt. Stuart (Matzel et al., 2006) taken from the 'alternative' flux estimates of Lipman and Bachmann (2015), as estimated by assuming an increase in total volume via a vertically extensive reservoir.

SRMVF: Southern Rocky Mountain Volcanic Field.

Figure 1

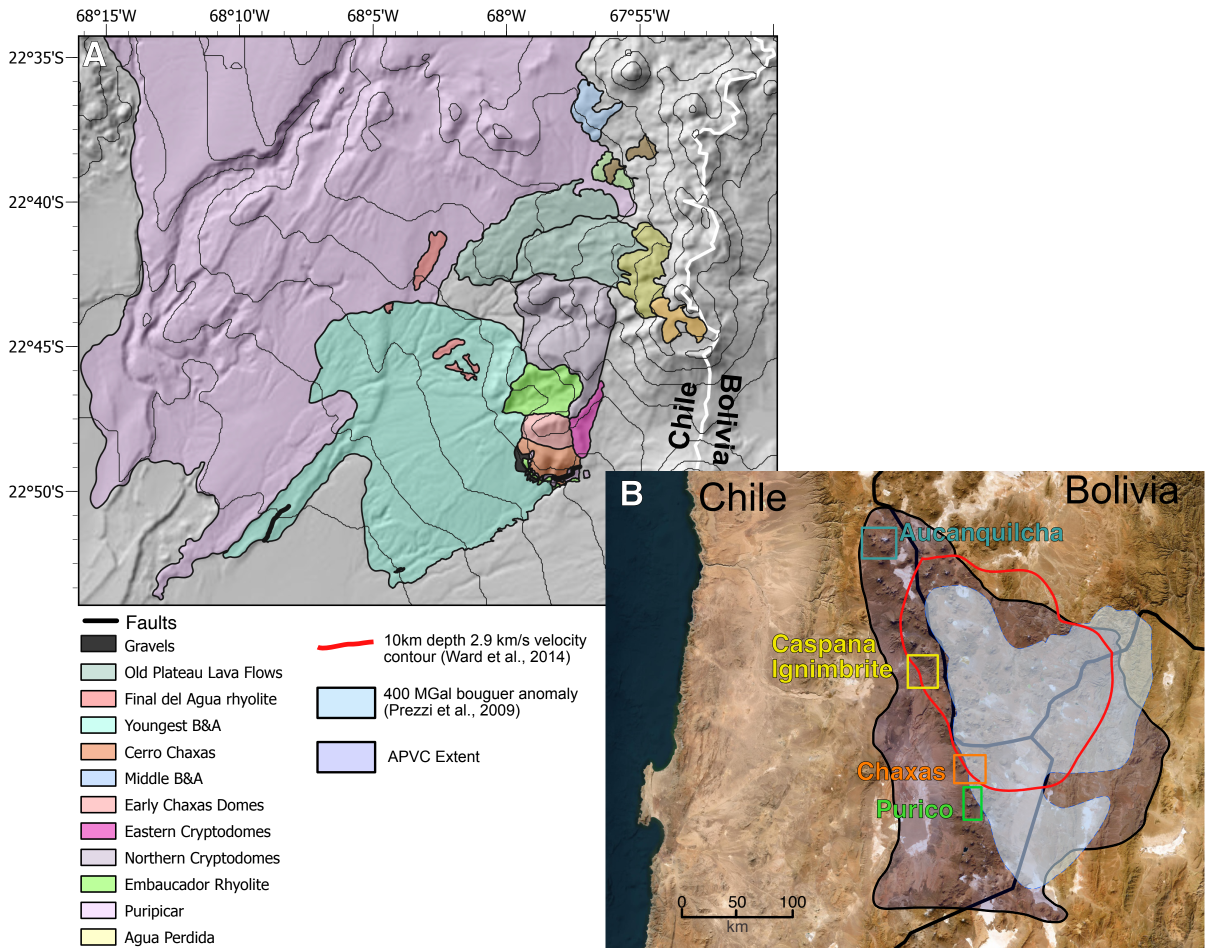

68°15'W
68°10'W
68°5'W
68°W
67°55'W
22°35'S
22°40'S
22°45'S
22°50'S
A
Chile
Bolivia
Faults
Gravels
Old Plateau Lava Flows
Final del Agua rhyolite
Youngest B&A
Cerro Chaxas
Middle B&A
Early Chaxas Domes
Eastern Cryptodomes
Northern Cryptodomes
Embaucador Rhyolite
Puripicar
Agua Perdida
10km depth 2.9 km/s velocity contour (Ward et al., 2014)
400 MGal bouguer anomaly (Prezzi et al., 2009)
APVC Extent
B
Chile
Bolivia
Aucanquilcha
Caspana Ignimbrite
Chaxas
Purico
0 50 100
km

Figure 2

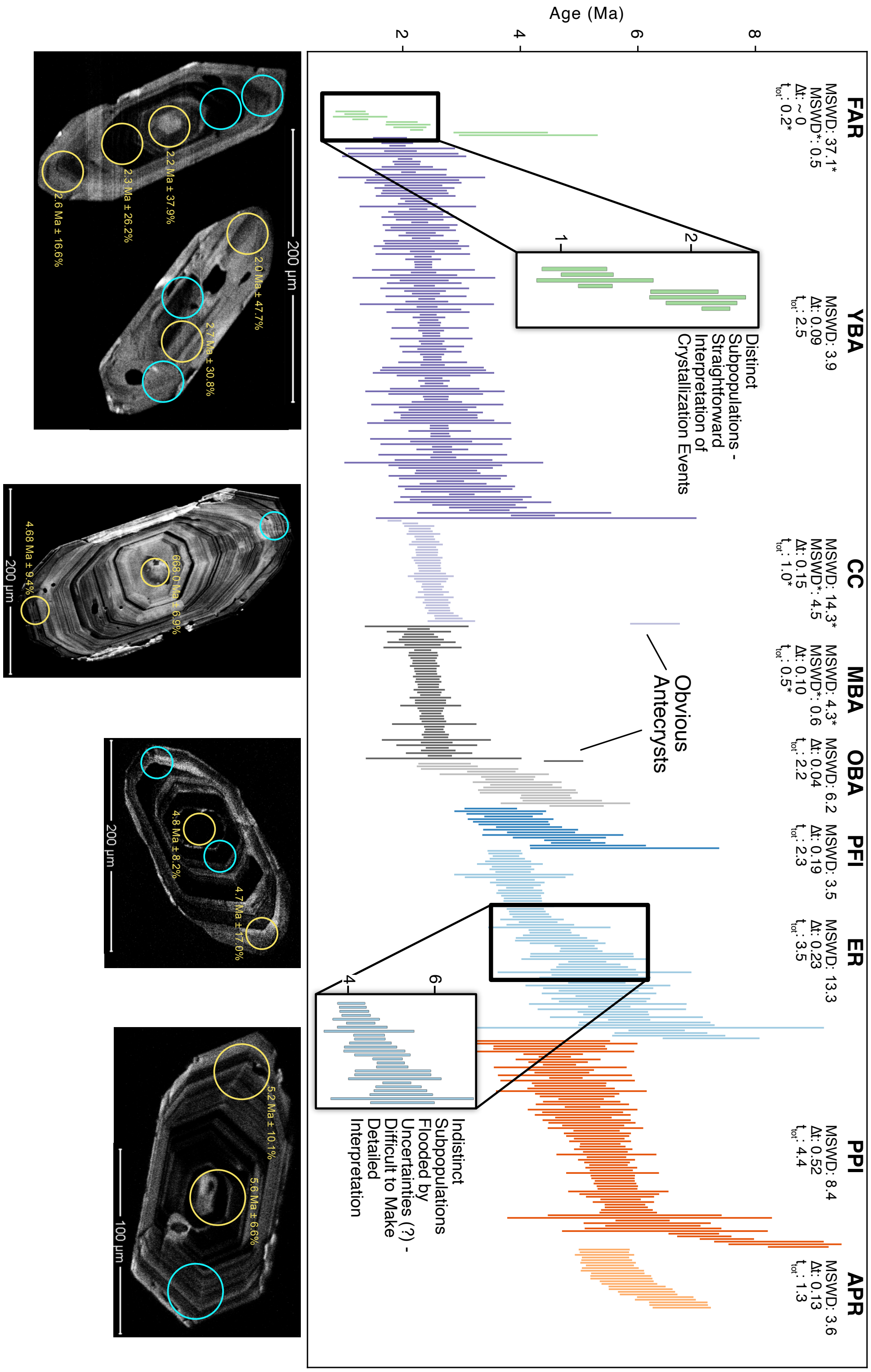
Age (Ma)
2
4
6
8
FAR
MSWD: 37.1*
MSWD*: 0.5
Δt: ~0
t_tot: 0.2*
YBA
MSWD: 3.9
Δt: 0.09
t_tot: 2.5
CC
MSWD: 14.3*
MSWD*: 4.5
Δt: 0.15
t_tot: 1.0*
MBA
MSWD: 4.3*
MSWD*: 0.6
Δt: 0.10
t_tot: 0.5*
OBA
MSWD: 6.2
Δt: 0.04
t_tot: 2.2
PFI
MSWD: 3.5
Δt: 0.19
t_tot: 2.3
ER
MSWD: 13.3
Δt: 0.23
t_tot: 3.5
PPI
MSWD: 8.4
Δt: 0.52
t_tot: 4.4
APR
MSWD: 3.6
Δt: 0.13
t_tot: 1.3
Distinct Subpopulations - Straightforward Interpretation of Crystallization Events
Obvious Antecrysts
Indistinct Subpopulations Flooded by Uncertainties (?) - Difficult to Make Detailed Interpretation
200 µm
200 µm
200 µm
100 µm

Figure 3

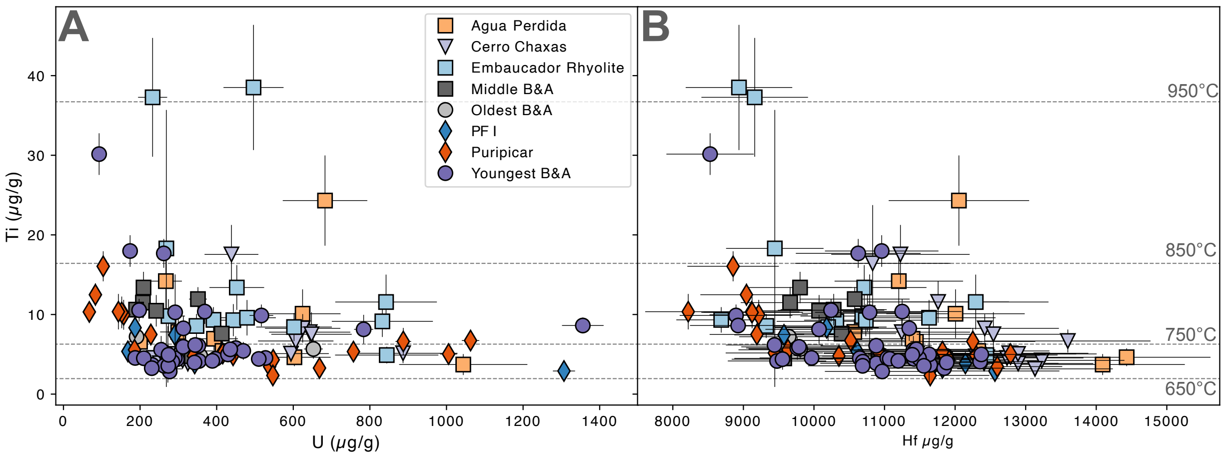
A
B
Agua Perdida
Cerro Chaxas
Embaucador Rhyolite
Middle B&A
Oldest B&A
PF I
Puripicar
Youngest B&A
Ti (μg/g)
U (μg/g)
Hf μg/g
950°C
850°C
750°C
650°C

Figure 4

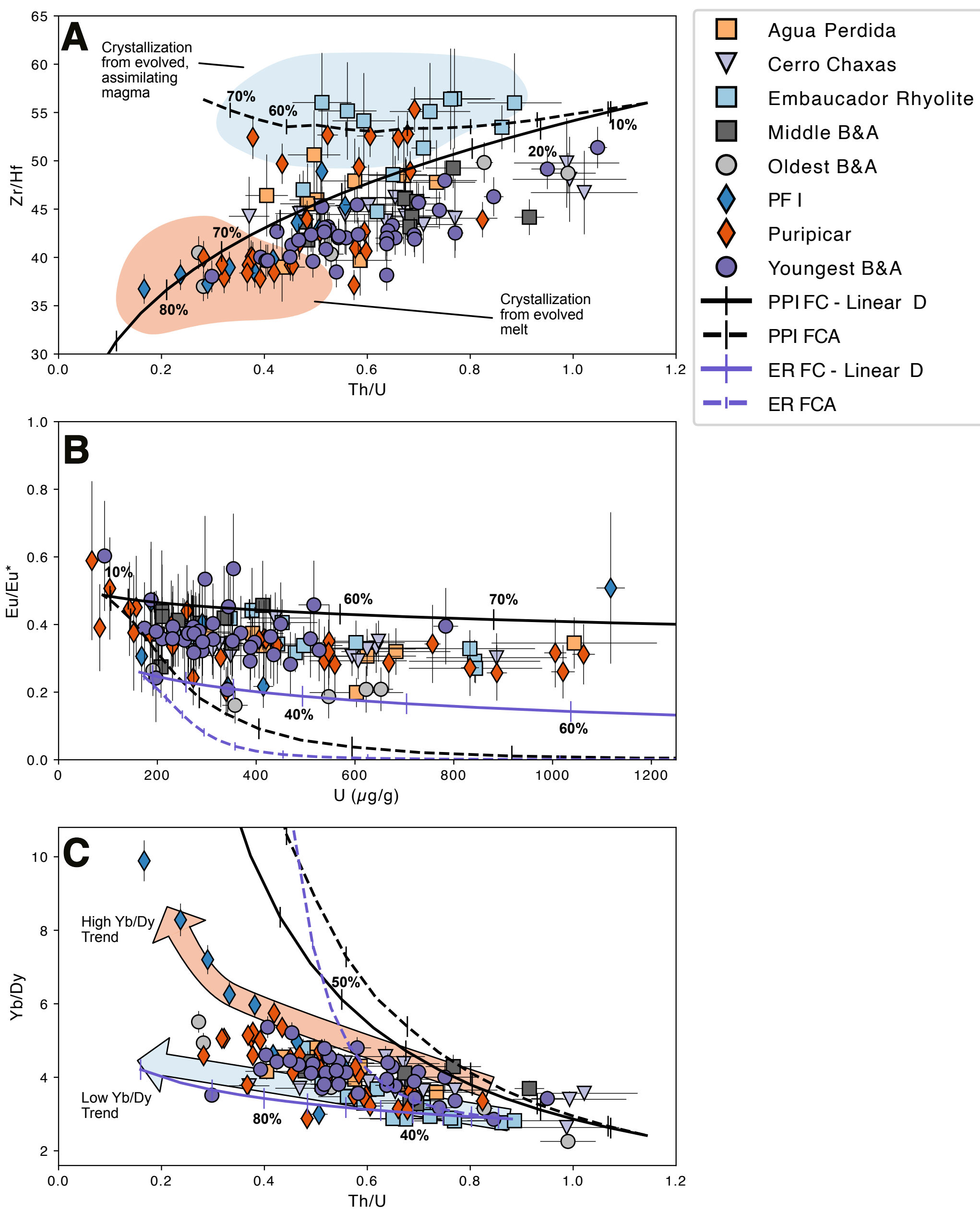
A
Crystallization from evolved, assimilating magma
Crystallization from evolved melt
70%
60%
10%
20%
70%
80%
Zr/Hf
Th/U
B
Eu/Eu*
U (μg/g)
10%
60%
70%
40%
60%
C
High Yb/Dy Trend
Low Yb/Dy Trend
50%
80%
40%
Yb/Dy
Th/U
Agua Perdida
Cerro Chaxas
Embaucador Rhyolite
Middle B&A
Oldest B&A
PF I
Puripicar
Youngest B&A
PPI FC - Linear D
PPI FCA
ER FC - Linear D
ER FCA

Figure 5

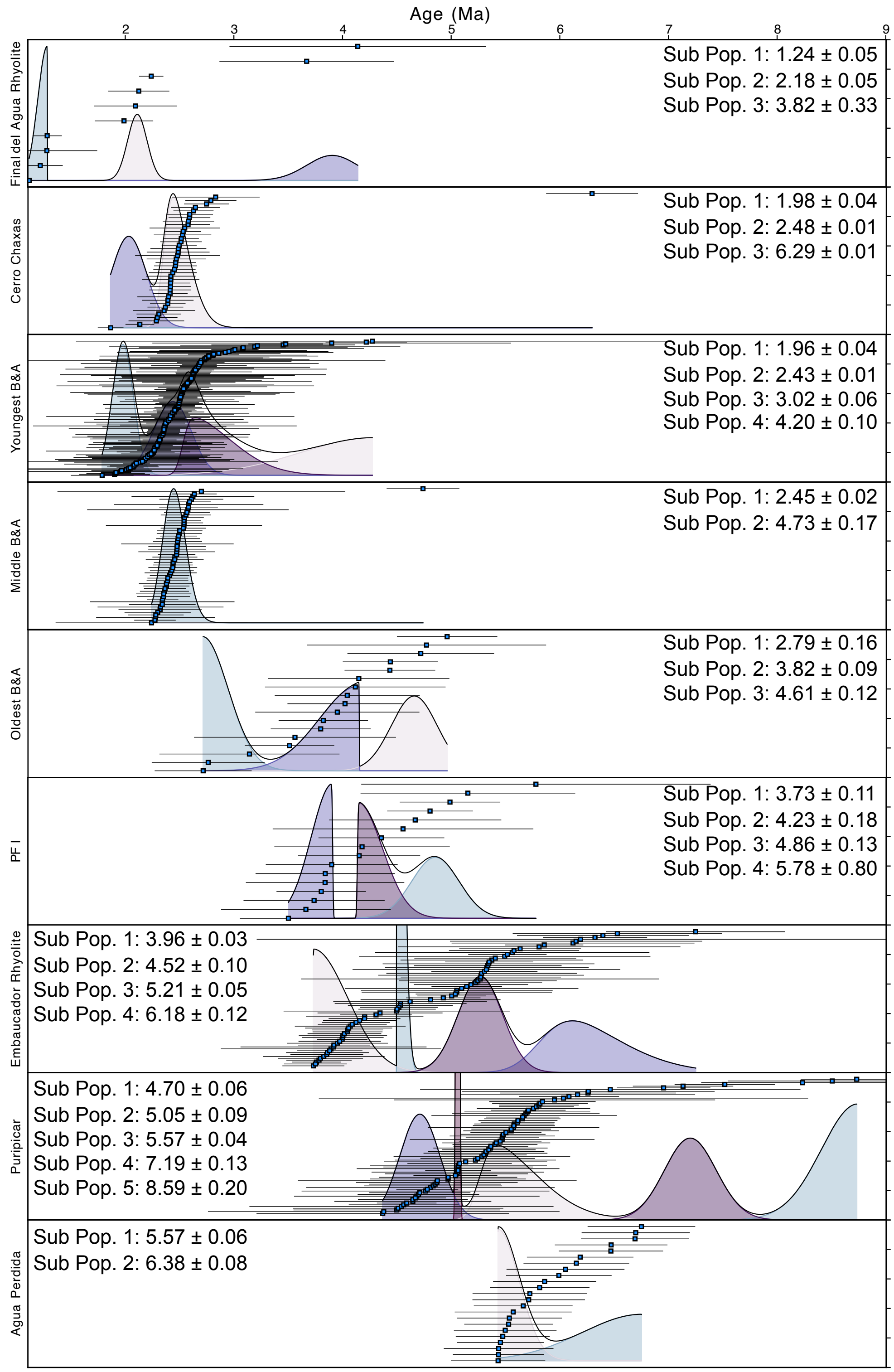

Age (Ma)
2
3
4
5
6
7
8
9
Final del Agua Rhyolite
Sub Pop. 1: 1.24 ± 0.05
Sub Pop. 2: 2.18 ± 0.05
Sub Pop. 3: 3.82 ± 0.33
Cerro Chaxas
Sub Pop. 1: 1.98 ± 0.04
Sub Pop. 2: 2.48 ± 0.01
Sub Pop. 3: 6.29 ± 0.01
Youngest B&A
Sub Pop. 1: 1.96 ± 0.04
Sub Pop. 2: 2.43 ± 0.01
Sub Pop. 3: 3.02 ± 0.06
Sub Pop. 4: 4.20 ± 0.10
Middle B&A
Sub Pop. 1: 2.45 ± 0.02
Sub Pop. 2: 4.73 ± 0.17
Oldest B&A
Sub Pop. 1: 2.79 ± 0.16
Sub Pop. 2: 3.82 ± 0.09
Sub Pop. 3: 4.61 ± 0.12
PF I
Sub Pop. 1: 3.73 ± 0.11
Sub Pop. 2: 4.23 ± 0.18
Sub Pop. 3: 4.86 ± 0.13
Sub Pop. 4: 5.78 ± 0.80
Embaucador Rhyolite
Sub Pop. 1: 3.96 ± 0.03
Sub Pop. 2: 4.52 ± 0.10
Sub Pop. 3: 5.21 ± 0.05
Sub Pop. 4: 6.18 ± 0.12
Puripicar
Sub Pop. 1: 4.70 ± 0.06
Sub Pop. 2: 5.05 ± 0.09
Sub Pop. 3: 5.57 ± 0.04
Sub Pop. 4: 7.19 ± 0.13
Sub Pop. 5: 8.59 ± 0.20
Agua Perdida
Sub Pop. 1: 5.57 ± 0.06
Sub Pop. 2: 6.38 ± 0.08

Figure 6

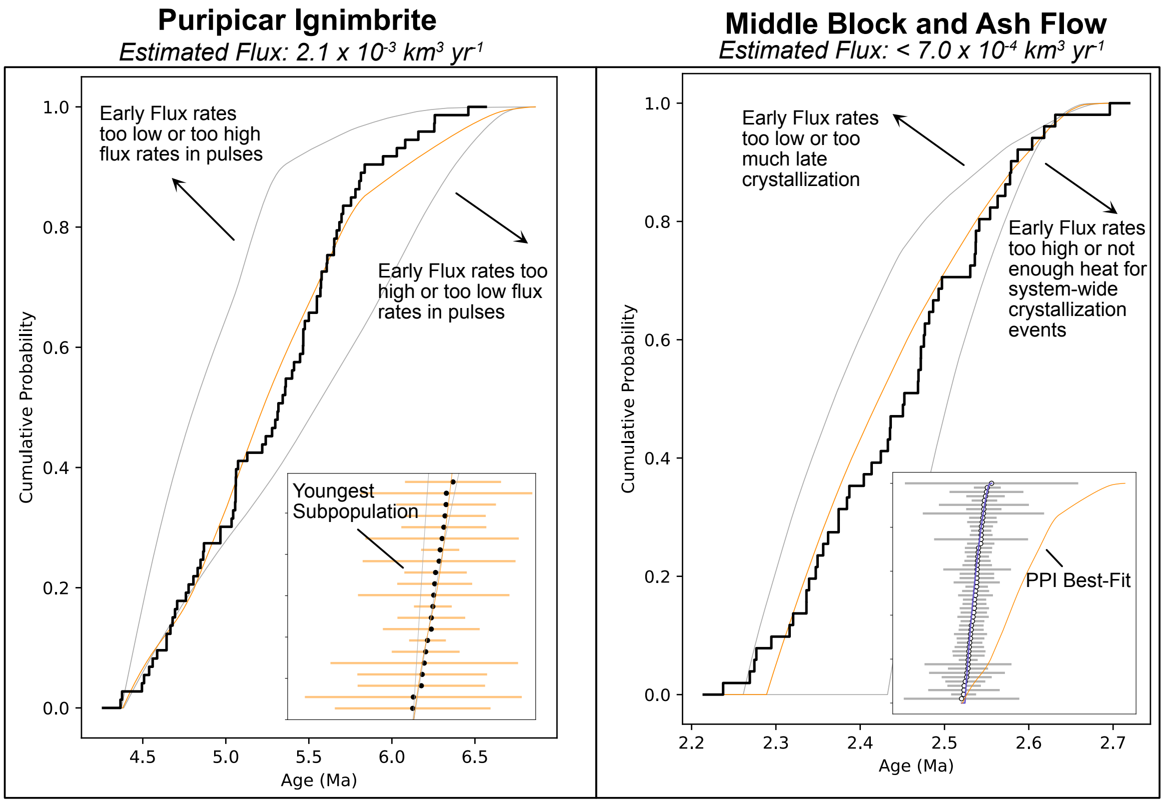

Puripicar Ignimbrite
Estimated Flux: 2.1 x 10-3 km3 yr-1
Early Flux rates too low or too high flux rates in pulses
Early Flux rates too high or too low flux rates in pulses
Youngest Subpopulation
Cumulative Probability
Age (Ma)
Middle Block and Ash Flow
Estimated Flux: < 7.0 x 10-4 km3 yr-1
Early Flux rates too low or too much late crystallization
Early Flux rates too high or not enough heat for system-wide crystallization events
PPI Best-Fit
Cumulative Probability
Age (Ma)

Figure 7

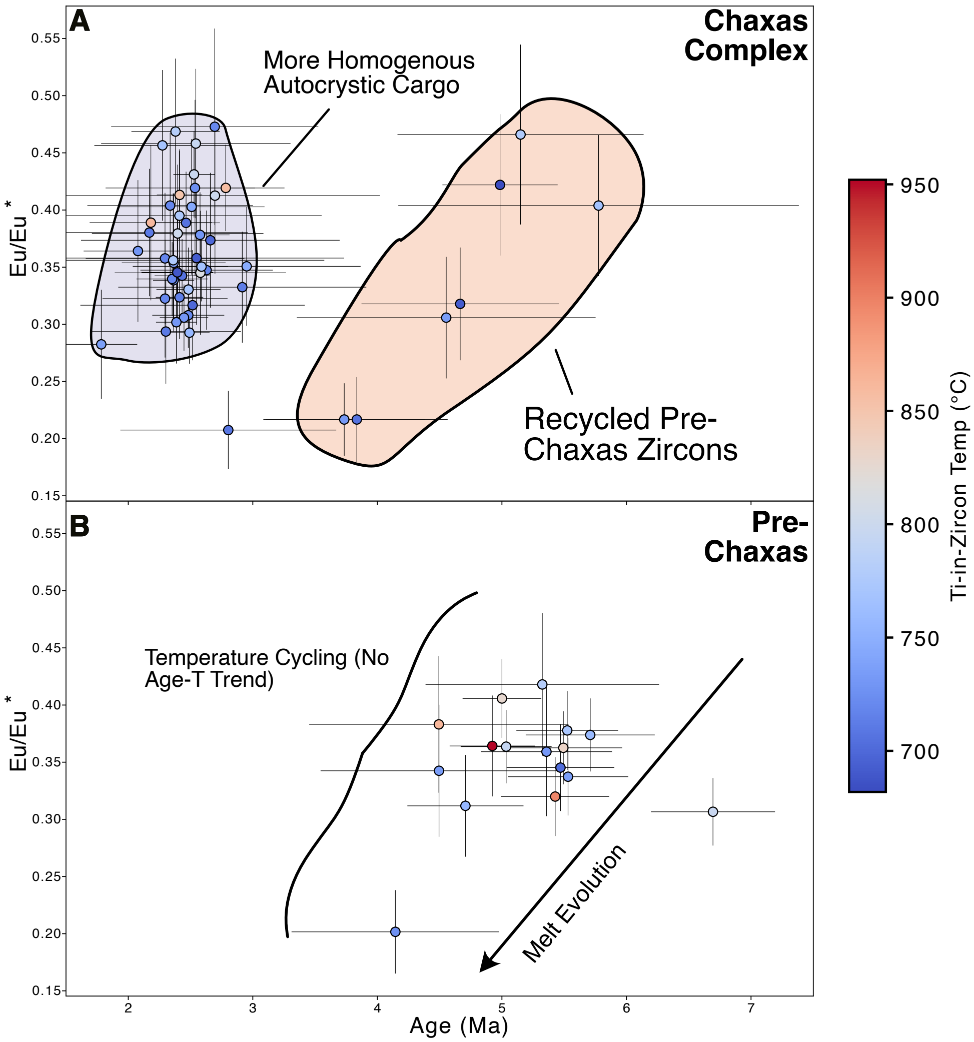
A
Chaxas Complex
More Homogenous Autocrystic Cargo
Recycled Pre-Chaxas Zircons
B
Pre-Chaxas
Temperature Cycling (No Age-T Trend)
Melt Evolution
Eu/Eu*
Age (Ma)
Ti-in-Zircon Temp (°C)
950
900
850
800
750
700

Figure 8

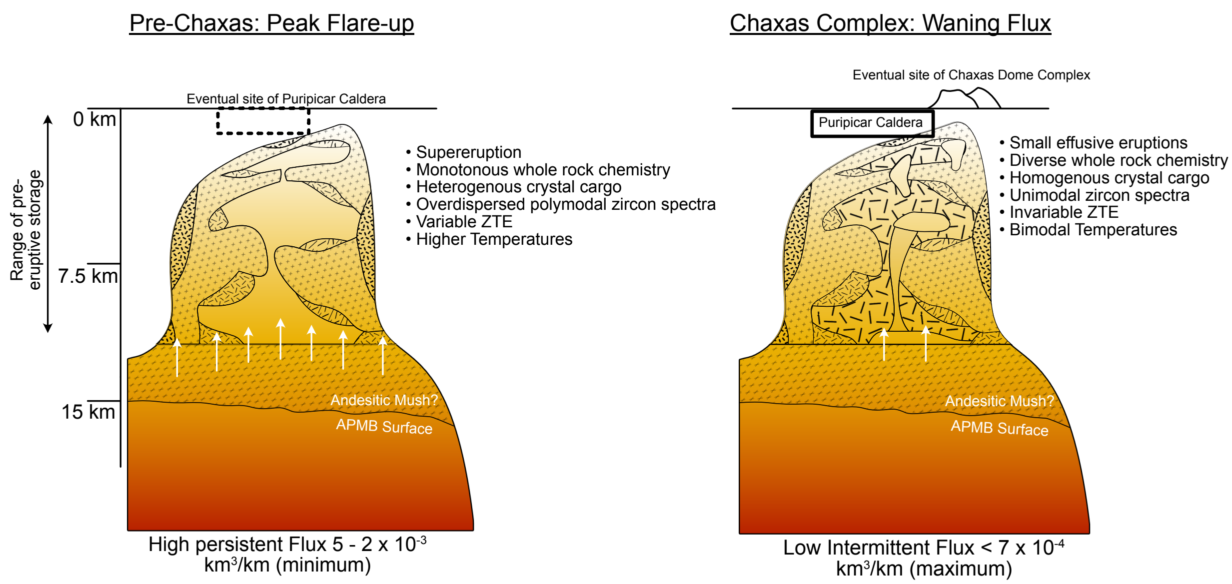
Pre-Chaxas: Peak Flare-up
Eventual site of Puripicar Caldera
0 km
7.5 km
15 km
Range of pre-eruptive storage
• Supereruption
• Monotonous whole rock chemistry
• Heterogenous crystal cargo
• Overdispersed polymodal zircon spectra
• Variable ZTE
• Higher Temperatures
Andesitic Mush?
APMB Surface
High persistent Flux 5 - 2 x 10-3 km3/km (minimum)
Chaxas Complex: Waning Flux
Eventual site of Chaxas Dome Complex
Puripicar Caldera
• Small effusive eruptions
• Diverse whole rock chemistry
• Homogenous crystal cargo
• Unimodal zircon spectra
• Invariable ZTE
• Bimodal Temperatures
Andesitic Mush?
APMB Surface
Low Intermittent Flux < 7 x 10-4 km3/km (maximum)

Figure Captions

Figure 1

A) Map of the Chaxas Volcanic Complex adapted from (Lewis et al., 2025) showing the extent of eruptive units. B) Regional map showing the extent of the APVC (purple region) and selected volcanic centers along the edge of the APVC. Light blue region shows the 400 MGal bouguer anomaly interpreted as presence of the APMB (Prezzi et al., 2009). Red line shows 2.9 km/s velocity contour from Ward et al. (2014).

Figure 2

Diagram showing rank order U-Pb zircon ages of eruptions of the Chaxas Volcanic Complex. Eruption age of units increases towards the right. Abbreviation of the unit, the MSWD, t_{tot}, and Δt are shown above each of the datasets (Table **1**). MSWD* and t_{tot}* indicates the MSWD and t_{tot} after removing the obvious antecrysts that are outside of the rest of the otherwise evenly dispersed population of U-Pb dates. FAR U-Pb dates show a case of clear discrimination between different subpopulations that facilitates a straightforward interpretation of multiple crystallization events or crystal scavenging. Samples like ER have clear perturbations in the extremely overdispersed datasets that are indicative of multiple underlying subpopulations that cannot be easily discriminated due to overlapping uncertainties, as shown in the blow-up diagram. Datasets such as these motivate the need to employ an approach that provides best estimates as to when major crystallization events occurred by using the data (c.f., Figure 5) and more sufficient calculation of Δt. CL-images below the diagram show representative zircon grains from this study with 30 μm spots superimposed. Yellow spots show location of U-Pb analyses with the determined date and uncertainty. Blue spots show location of trace element analyses.

Figure 3

Zircon Ti concentrations vs U and Hf concentrations. Dashed lines show Ti concentration at a given temperature (Ferry and Watson, 2007). A general increase in Hf and U concentration with decreasing temperature is present, although a wide variety of temperatures at fairly low degrees of evolution imply thermal gradients were present in the magmatic reservoir. Most evolved, high U zircons come from the APR, ER, and PPI. Note the consistently high Ti concentrations in MBA and the thermal bimodality suggested by YBA zircons.

Figure 4

Zircon trace element analyses for each eruptive unit with modeled fractional crystallization (FC) and fractional crystallization and assimilation (FCA) trends. Solid and dashed lines show FC and FCA trends, respectively. Solid black numbers show percentage of melt remaining in the model. Black and purple models show modeled trends using the PPI and ER as starting compositions, respectively. A) Zr/Hf vs Th/U values. Note that decreasing Zr/Hf values are interpreted to indicate progressive melt evolution, but the evolved ER, APR, and PPI carry the highest Zr/Hf that are best explained by assimilation of high Zr/Hf melt. B) Eu/Eu* vs U concentrations. Models here bracket the data array, supporting that melt evolution formed progressively high U, low Eu/Eu zircons. C) Yb/Dy vs Th/U values. Two distinct trends defining a low and high Yb/Dy trend are interpreted from the dataset. Lower trend formed primarily by ER zircons is best explained by FC of rhyolitic melt. All other data fall between the models that describe melt evolution within the system.

Figure 5

Rank order U-Pb zircon crystallization ages with distributions of U-Pb subpopulations representing periods of major crystallization events. Age of eruptive unit increases towards the top. Black solid lines show KDE of the entire populations. Truncation of the skew normal distributions results from the estimated distribution parameters and in some cases the distributions are nearly half-normal, which closely approximates the theoretical distribution of zircon ages and would be expected by crystallization interrupted by eruption or instantaneous nucleation. Broader distributions approximating a normal distribution have large tails, indicating high variance due to either large measurement uncertainty or an extended duration of crystallization. Note the overlap of subpopulations in younger units with those in older units. Weighted mean and uncertainty of U-Pb crystallization ages from each subpopulation are also shown in each panel.

Figure 6

Diagrams showing cumulative probability of U-Pb zircon crystallization ages (black lines) with poorly fit synthetic zircon distributions (grey lines) and best fit synthetic zircon distributions (orange lines) from thermal models used to predict the flux (Table 2). PPI is representative of the high-flux regime that produced the PPI supereruption during the Pre-Chaxas stage, whereas MBA represents the low flux regime during the Chaxas Complex stage. Note the flux estimate for the MBA is a maximum as the age data are underdispersed. Inset diagram on PPI panel shows youngest subpopulation resolved by skew-normal mixture modeling, emphasizing the fit of the highest flux model shown in orange. Inset diagram on MBA panel shows MBA data (excluding obvious antecrysts; c.f., Figure 2) with best fit low flux model shown as purple line with the best-fit. Best fit PPI model shown in orange is an extreme misfit due to higher flux associated with that model.

<u>Figure 7</u>

Eu/Eu* vs U-Pb zircon crystallization ages from zircons in Chaxas Complex eruptions (A) and Pre-Chaxas eruptions (B). Pre-Chaxas zircons show progressive melt evolution with no systematic correlation of Ti-in-zircon crystallization temperature, indicating large temperature cycling during high-flux. Chaxas Complex zircons show more homogenous trace element chemistry indicating more invariable melt composition in the autocrystic zircon population in the light purple field. Antecrystic zircon population show low Ti-in-zircon crystallization temperatures indicating extensive cannibalization of low temperature material emplaced millions of years earlier during the Pre-Chaxas eruptions.

<u>Figure 8</u>

Schematic diagram illustrating a generalized physical representation based on the temporal, thermal, geochemical, and modeled results of the Chaxas Volcanic Complex magmatic system. Upper surface of APMB from Pritchard et al. (2018). Depth range of pre-eruption storage estimated from PT conditions estimated for the APVC previously (Grocke et al., 2017; Lindsay et al., 2001). Pre-Chaxas shows run-up to 4.18 Ma Puripicar supereruption during high flux conditions that formed large volumes of monotonous dacite. Subsequent low flux magmatism from 3.54 – 1.24 Ma that characterized the Chaxas Complex depicts smaller discrete bodies of short lived melt within the Pre-Chaxas mush. Color gradient represents thermal gradient from the APMB. Surface volcanic features exaggerated for clarity.

Compositional Data

Unit	sample	Material	zr	th	u	sm
Embaucador	CHX22015	Whole Rock	109	19.73	7.47	5.28
PPI	CHX22-21	Whole Rock Low Sr	156	13.99	4.08	5.18
Xenolith Glas	BC93PAX12	Mcleod et al Xenolith	102.5	3.3	1.5	4.3

Partition Coefficients D Values

	zr	th	u	sm
Quartz				
Plagioclse	0.004	0	0	0
Sanidine	0.005	0	0	0
Biotite	0.052	0.016	0	0
Amphibole	0.397	0.036	0.073	8.1
Orthopyroxene				
Zircon	6034	7.33	22	1.13
Apatite	1.62	5.13	2.07	253
Allanite-Chevkinite	0.13	271	6.82	1607

Bulk D from approximate mineralogy

Mineral %'s	Puripicar		D-values			
Quartz	15.08		0.0	0.0	0.0	0.0
Plagioclse	60.32		0.0	0.0	0.0	0.0
Sanidine	0.00		0.0	0.0	0.0	0.0
Biotite	15.08		0.0	0.0	0.0	0.0
Amphibole	8.04		0.0	0.0	0.0	0.7
Orthopyroxei	0.00		0.0	0.0	0.0	0.0
Zircon	0.03		1.5	0.0	0.0	0.0
Apatite	1.01		0.0	0.1	0.0	2.5
Allanite-Che	0.45		0.0	1.2	0.0	7.3
		Bulk-D	*1.6*	*1.3*	*0.1*	*10.5*
	ER					
Quartz	25.8		0.0	0.0	0.0	0.0
Plagioclse	51.5		0.0	0.0	0.0	0.0
Sanidine	8.6		0.0	0.0	0.0	0.0
Biotite	12.9		0.0	0.0	0.0	0.0
Amphibole	0.0		0.0	0.0	0.0	0.0
Orthopyroxei	0.0		0.0	0.0	0.0	0.0
Zircon	0.2		10.4	0.0	0.0	0.0
Apatite	0.9		0.0	0.0	0.0	2.2
Allanite-Che	0.2		0.0	0.6	0.0	3.4
		Bulk-D	*10.4*	*0.6*	*0.1*	*5.6*

PPI **Fractionation Models**

	zr	th	u	sm
b-values				

Linear D Fractionation	F		1	-2	-2	-4
Greenland (1970)		0.05	1.1E+01	4.0E+01	4.5E+02	1.1E-10
Equation 14		0.1	1.7E+01	4.4E+01	2.1E+02	6.5E-08
		0.15	2.2E+01	4.5E+01	1.3E+02	2.5E-06
		0.2	2.8E+01	4.4E+01	9.1E+01	3.1E-05
		0.25	3.3E+01	4.2E+01	6.7E+01	2.1E-04
		0.3	3.9E+01	4.0E+01	5.1E+01	9.6E-04
		0.35	4.5E+01	3.8E+01	4.0E+01	3.4E-03
		0.4	5.1E+01	3.6E+01	3.2E+01	9.8E-03
		0.45	5.7E+01	3.3E+01	2.6E+01	2.4E-02
		0.5	6.4E+01	3.1E+01	2.1E+01	5.4E-02
		0.55	7.1E+01	2.9E+01	1.8E+01	1.1E-01
		0.6	7.8E+01	2.7E+01	1.5E+01	2.0E-01
		0.65	8.6E+01	2.5E+01	1.2E+01	3.6E-01
		0.7	9.4E+01	2.3E+01	1.0E+01	5.9E-01
		0.75	1.0E+02	2.1E+01	8.8E+00	9.2E-01
		0.8	1.1E+02	2.0E+01	7.5E+00	1.4E+00
		0.85	1.2E+02	1.8E+01	6.4E+00	2.0E+00
		0.9	1.3E+02	1.7E+01	5.5E+00	2.9E+00
		0.95	1.4E+02	1.5E+01	4.7E+00	3.9E+00
		1	1.6E+02	1.4E+01	4.1E+00	5.2E+00

FCA	R					
Cribb and Barton (1996)		0.1	2.1E+02	4.6E+01	4.5E+02	8.2E+00
Equation 6		0.1	1.1E+02	4.7E+01	2.1E+02	3.9E+00
		0.1	8.1E+01	4.6E+01	1.3E+02	2.4E+00
		0.1	6.9E+01	4.5E+01	9.2E+01	1.7E+00
		0.1	6.4E+01	4.3E+01	6.7E+01	1.3E+00
		0.6	1.8E+02	4.5E+01	5.3E+01	6.0E+00
		0.6	1.6E+02	4.2E+01	4.2E+01	4.8E+00
		0.6	1.4E+02	3.9E+01	3.3E+01	3.9E+00
		0.6	1.3E+02	3.6E+01	2.7E+01	3.2E+00
		0.7	1.4E+02	3.4E+01	2.2E+01	3.1E+00
		0.7	1.3E+02	3.1E+01	1.8E+01	2.6E+00
		0.7	1.3E+02	2.8E+01	1.5E+01	2.2E+00
		0.8	1.3E+02	2.6E+01	1.3E+01	2.2E+00
		0.8	1.3E+02	2.4E+01	1.1E+01	2.1E+00
		0.8	1.3E+02	2.2E+01	9.2E+00	2.1E+00
		0.8	1.3E+02	2.0E+01	7.8E+00	2.3E+00
		0.8	1.4E+02	1.8E+01	6.6E+00	2.6E+00
		0.9	1.4E+02	1.7E+01	5.7E+00	3.3E+00
		0.9	1.5E+02	1.5E+01	4.8E+00	4.1E+00
		0.9	1.6E+02	1.4E+01	4.1E+00	5.2E+00

ER

Rayleigh Fractionation F

0.05	6.7E-11	5.8E+01	1.2E+02	5.1E-06
0.1	4.5E-08	4.5E+01	6.4E+01	1.3E-04
0.15	2.0E-06	3.9E+01	4.4E+01	8.2E-04
0.2	3.0E-05	3.5E+01	3.3E+01	3.1E-03
0.25	2.4E-04	3.2E+01	2.7E+01	8.7E-03
0.3	1.3E-03	3.0E+01	2.3E+01	2.0E-02
0.35	5.7E-03	2.9E+01	2.0E+01	4.1E-02
0.4	2.0E-02	2.7E+01	1.8E+01	7.6E-02
0.45	6.1E-02	2.6E+01	1.6E+01	1.3E-01
0.5	1.6E-01	2.5E+01	1.4E+01	2.1E-01
0.55	4.0E-01	2.4E+01	1.3E+01	3.3E-01
0.6	9.0E-01	2.4E+01	1.2E+01	5.0E-01
0.65	1.9E+00	2.3E+01	1.1E+01	7.2E-01
0.7	3.8E+00	2.2E+01	1.0E+01	1.0E+00
0.75	7.3E+00	2.2E+01	9.8E+00	1.4E+00
0.8	1.3E+01	2.1E+01	9.2E+00	1.9E+00
0.85	2.4E+01	2.1E+01	8.7E+00	2.5E+00
0.9	4.1E+01	2.0E+01	8.2E+00	3.2E+00
0.95	6.7E+01	2.0E+01	7.8E+00	4.2E+00
1	1.1E+02	2.0E+01	7.5E+00	5.3E+00

Linear D Fractionation
Greenland (1970)
Equation 14

b-values

1	-2	-2	-4
2.587E-11	387.244932	809.087087	0.00022714
1.8204E-08	273.108634	384.298487	0.00458725
8.6058E-07	213.599796	238.511812	0.02449246
1.3467E-05	174.283257	165.16295	0.07585005
0.00011498	145.541512	121.444102	0.17428492
0.00066925	123.336501	92.7522385	0.33157105
0.00299026	105.583165	72.7190082	0.55375141
0.01100961	91.05777	58.1162644	0.84070027
0.03496522	78.9765452	47.1310071	1.18669316
0.0988233	68.8048064	38.6662487	1.58156202
0.25416264	60.160104	32.0195886	2.01209675
0.60469098	52.7586981	26.7208681	2.46345214
1.3475568	46.3839337	22.4439541	2.92040767
2.84032059	40.8665215	18.9559111	3.36839857
5.70605078	36.0716815	16.0862741	3.79428781
10.9937404	31.8904436	13.7077116	4.18688394
20.4173833	28.2335707	11.7234358	4.53723084
36.7049368	25.0271982	10.0587622	4.83870646
64.0984386	22.209628	8.65530568	5.08697154
109.059208	19.7289254	7.4669013	5.27980846

FCA R

Cribb and Ba	0.3	5.8E+02	7.7E+01	1.3E+02	2.5E+01
Equation 6	0.3	2.8E+02	5.4E+01	6.8E+01	1.2E+01
	0.3	1.7E+02	4.5E+01	4.6E+01	7.3E+00
	0.3	1.2E+02	3.9E+01	3.5E+01	5.2E+00
	0.3	9.2E+01	3.5E+01	2.8E+01	3.9E+00
	0.3	7.2E+01	3.3E+01	2.4E+01	3.0E+00
	0.3	5.7E+01	3.1E+01	2.1E+01	2.4E+00
	0.3	4.6E+01	2.9E+01	1.8E+01	2.0E+00
	0.3	3.8E+01	2.7E+01	1.6E+01	1.7E+00
	0.3	3.1E+01	2.6E+01	1.5E+01	1.5E+00
	0.3	2.6E+01	2.5E+01	1.3E+01	1.4E+00
	0.3	2.1E+01	2.4E+01	1.2E+01	1.4E+00
	0.3	1.8E+01	2.4E+01	1.1E+01	1.4E+00
	0.3	1.7E+01	2.3E+01	1.1E+01	1.6E+00
	0.3	1.8E+01	2.2E+01	9.9E+00	1.8E+00
	0.3	2.1E+01	2.2E+01	9.3E+00	2.2E+00
	0.3	2.9E+01	2.1E+01	8.8E+00	2.7E+00
	0.3	4.4E+01	2.1E+01	8.3E+00	3.4E+00
	0.3	6.9E+01	2.0E+01	7.9E+00	4.2E+00
	0.3	1.1E+02	2.0E+01	7.5E+00	5.3E+00

eu	gd	yb	hf	zr	th
0.63	4.29	2.26	3.89		
1.13	4.02	1.56	4.38		
		0.7	2.5		

3.36	0	0	0
2.33	0	0	0
0	0	0	0
6.32	7.33	4.6	0.821
2.52	13.46	353	3850
152	230	232	15
1028	829	158	18.9

Sources
Padilla and Gualda 2016
Ewart and Griffin (1994)
Claiborne et al (2018)

0.0	0.0	0.0	0.0
2.0	0.0	0.0	0.0
0.0	0.0	0.0	0.0
0.0	0.0	0.0	0.0
0.5	0.6	0.4	0.1
0.0	0.0	0.0	0.0
0.0	0.0	0.1	1.0
1.5	2.3	2.3	0.2
4.7	3.8	0.7	0.1
8.7	*6.7*	*3.5*	*1.3*
0.0	0.0	0.0	0.0
1.7	0.0	0.0	0.0
0.2	0.0	0.0	0.0
0.0	0.0	0.0	0.0
0.0	0.0	0.0	0.0
0.0	0.0	0.0	0.0
0.0	0.0	0.6	6.6
1.3	2.0	2.0	0.1
2.2	1.8	0.3	0.0
5.4	*3.8*	*2.9*	*6.8*

eu	gd	yb	hf	zr	th

-4	-4	-4	1		
4.6E-09	7.9E-06	3.8E-02	7.5E-01	6.5E+04	2.9E+02
8.0E-07	3.3E-04	1.8E-01	9.6E-01	1.0E+05	3.2E+02
1.5E-05	2.6E-03	4.0E-01	1.1E+00	1.4E+05	3.3E+02
1.1E-04	1.1E-02	6.8E-01	1.3E+00	1.7E+05	3.2E+02
5.1E-04	3.2E-02	9.7E-01	1.4E+00	2.0E+05	3.1E+02
1.7E-03	7.3E-02	1.3E+00	1.6E+00	2.3E+05	3.0E+02
4.6E-03	1.4E-01	1.5E+00	1.7E+00	2.7E+05	2.8E+02
1.1E-02	2.5E-01	1.7E+00	1.9E+00	3.1E+05	2.6E+02
2.2E-02	4.0E-01	1.9E+00	2.0E+00	3.4E+05	2.5E+02
4.0E-02	5.9E-01	2.0E+00	2.2E+00	3.8E+05	2.3E+02
6.8E-02	8.3E-01	2.1E+00	2.4E+00	4.3E+05	2.1E+02
1.1E-01	1.1E+00	2.2E+00	2.6E+00	4.7E+05	2.0E+02
1.7E-01	1.4E+00	2.2E+00	2.7E+00	5.2E+05	1.8E+02
2.4E-01	1.8E+00	2.1E+00	2.9E+00	5.7E+05	1.7E+02
3.3E-01	2.1E+00	2.1E+00	3.2E+00	6.2E+05	1.6E+02
4.5E-01	2.5E+00	2.0E+00	3.4E+00	6.8E+05	1.4E+02
5.9E-01	2.9E+00	1.9E+00	3.6E+00	7.4E+05	1.3E+02
7.5E-01	3.3E+00	1.8E+00	3.8E+00	8.0E+05	1.2E+02
9.3E-01	3.7E+00	1.7E+00	4.1E+00	8.7E+05	1.1E+02
1.1E+00	4.0E+00	1.6E+00	4.4E+00	9.4E+05	1.0E+02

4.6E-09	7.9E-06	1.4E+00	5.5E+00	1.2E+06	3.4E+02
8.0E-07	3.3E-04	8.1E-01	3.2E+00	6.6E+05	3.4E+02
1.5E-05	2.6E-03	8.0E-01	2.5E+00	4.9E+05	3.4E+02
1.1E-04	1.1E-02	9.6E-01	2.3E+00	4.2E+05	3.3E+02
5.1E-04	3.2E-02	1.2E+00	2.2E+00	3.9E+05	3.2E+02
1.7E-03	7.3E-02	2.2E+00	5.1E+00	1.1E+06	3.3E+02
4.6E-03	1.4E-01	2.3E+00	4.5E+00	9.6E+05	3.1E+02
1.1E-02	2.5E-01	2.4E+00	4.1E+00	8.6E+05	2.8E+02
2.2E-02	4.0E-01	2.4E+00	3.9E+00	8.0E+05	2.6E+02
4.0E-02	5.9E-01	2.5E+00	4.0E+00	8.2E+05	2.5E+02
6.8E-02	8.3E-01	2.5E+00	3.8E+00	7.8E+05	2.3E+02
1.1E-01	1.1E+00	2.5E+00	3.7E+00	7.6E+05	2.1E+02
1.7E-01	1.4E+00	2.5E+00	3.8E+00	7.9E+05	1.9E+02
2.4E-01	1.8E+00	2.4E+00	3.8E+00	7.8E+05	1.8E+02
3.3E-01	2.1E+00	2.3E+00	3.8E+00	7.9E+05	1.6E+02
4.5E-01	2.5E+00	2.1E+00	3.9E+00	8.0E+05	1.5E+02
5.9E-01	2.9E+00	2.0E+00	4.0E+00	8.3E+05	1.4E+02
7.5E-01	3.3E+00	1.9E+00	4.1E+00	8.7E+05	1.2E+02
9.3E-01	3.7E+00	1.7E+00	4.2E+00	9.0E+05	1.1E+02
1.1E+00	4.0E+00	1.6E+00	4.4E+00	9.4E+05	1.0E+02

1.0E-06	1.0E-03	6.8E-03	1.2E-07	4.0E-07	4.2E+02
2.2E-05	7.2E-03	2.6E-02	6.4E-06	2.7E-04	3.3E+02
1.4E-04	2.2E-02	5.7E-02	6.7E-05	1.2E-02	2.9E+02
4.9E-04	4.9E-02	1.0E-01	3.5E-04	1.8E-01	2.6E+02
1.3E-03	9.1E-02	1.5E-01	1.3E-03	1.5E+00	2.4E+02
3.0E-03	1.5E-01	2.2E-01	3.7E-03	8.1E+00	2.2E+02
5.9E-03	2.3E-01	3.0E-01	9.0E-03	3.5E+01	2.1E+02
1.1E-02	3.4E-01	3.8E-01	1.9E-02	1.2E+02	2.0E+02
1.8E-02	4.7E-01	4.8E-01	3.8E-02	3.7E+02	1.9E+02
2.9E-02	6.3E-01	5.9E-01	7.1E-02	9.8E+02	1.9E+02
4.4E-02	8.2E-01	7.1E-01	1.2E-01	2.4E+03	1.8E+02
6.5E-02	1.0E+00	8.4E-01	2.0E-01	5.4E+03	1.7E+02
9.2E-02	1.3E+00	9.8E-01	3.2E-01	1.2E+04	1.7E+02
1.3E-01	1.6E+00	1.1E+00	5.0E-01	2.3E+04	1.6E+02
1.7E-01	1.9E+00	1.3E+00	7.4E-01	4.4E+04	1.6E+02
2.3E-01	2.3E+00	1.5E+00	1.1E+00	8.1E+04	1.6E+02
3.0E-01	2.7E+00	1.7E+00	1.5E+00	1.4E+05	1.5E+02
3.9E-01	3.2E+00	1.8E+00	2.1E+00	2.4E+05	1.5E+02
5.0E-01	3.7E+00	2.1E+00	2.9E+00	4.1E+05	1.5E+02
6.3E-01	4.3E+00	2.3E+00	3.9E+00	6.6E+05	1.4E+02

-4	-4	-4	1		
4.5715E-05	0.04666222	0.30493632	4.5253E-08	1.6E-07	2.8E+03
0.00081685	0.26203061	0.95646388	2.6171E-06	1.1E-04	2.0E+03
0.0040599	0.66170652	1.71802319	2.8683E-05	5.2E-03	1.6E+03
0.01194997	1.20470243	2.45623041	0.00015911	8.1E-02	1.3E+03
0.02639676	1.83329279	3.09882294	0.00060774	6.9E-01	1.1E+03
0.04862721	2.49077379	3.61219057	0.00183328	4.0E+00	9.0E+02
0.07902978	3.12932064	3.98691826	0.00469903	1.8E+01	7.7E+02
0.11718507	3.71269916	4.22816415	0.01069087	6.6E+01	6.7E+02
0.1620067	4.21628434	4.34923936	0.02220621	2.1E+02	5.8E+02
0.21193235	4.62575798	4.36737619	0.04292831	6.0E+02	5.0E+02
0.26512305	4.93526778	4.30100582	0.07830277	1.5E+03	4.4E+02
0.31964436	5.14548679	4.1680757	0.13613591	3.6E+03	3.9E+02
0.37361589	5.2618066	3.98507664	0.2273371	8.1E+03	3.4E+02
0.42532372	5.29277399	3.76654689	0.36683108	1.7E+04	3.0E+02
0.4732963	5.24880838	3.52488915	0.57466957	3.4E+04	2.6E+02
0.51634767	5.14119584	3.27038581	0.87737578	6.6E+04	2.3E+02
0.55359342	4.98133402	3.01133291	1.30956028	1.2E+05	2.1E+02
0.58444547	4.78019246	2.75423862	1.91585169	2.2E+05	1.8E+02
0.60859148	4.54795062	2.5040498	2.75319177	3.9E+05	1.6E+02
0.62596405	4.29377716	2.26438339	3.89355093	6.6E+05	1.4E+02

1.0E-06	1.0E-03	4.0E+00	1.4E+01	3.5E+06	5.6E+02
2.2E-05	7.2E-03	1.9E+00	6.8E+00	1.7E+06	4.0E+02
1.4E-04	2.2E-02	1.2E+00	4.3E+00	1.1E+06	3.3E+02
4.9E-04	4.9E-02	9.4E-01	3.0E+00	7.4E+05	2.9E+02
1.3E-03	9.1E-02	7.8E-01	2.3E+00	5.6E+05	2.6E+02
3.0E-03	1.5E-01	7.1E-01	1.8E+00	4.3E+05	2.4E+02
5.9E-03	2.3E-01	6.9E-01	1.4E+00	3.4E+05	2.2E+02
1.1E-02	3.4E-01	7.0E-01	1.1E+00	2.8E+05	2.1E+02
1.8E-02	4.7E-01	7.4E-01	9.6E-01	2.3E+05	2.0E+02
2.9E-02	6.3E-01	8.0E-01	8.2E-01	1.9E+05	1.9E+02
4.4E-02	8.2E-01	8.8E-01	7.4E-01	1.5E+05	1.9E+02
6.5E-02	1.0E+00	9.8E-01	7.0E-01	1.3E+05	1.8E+02
9.2E-02	1.3E+00	1.1E+00	7.3E-01	1.1E+05	1.7E+02
1.3E-01	1.6E+00	1.2E+00	8.2E-01	1.0E+05	1.7E+02
1.7E-01	1.9E+00	1.4E+00	9.9E-01	1.1E+05	1.6E+02
2.3E-01	2.3E+00	1.5E+00	1.3E+00	1.3E+05	1.6E+02
3.0E-01	2.7E+00	1.7E+00	1.7E+00	1.8E+05	1.5E+02
3.9E-01	3.2E+00	1.9E+00	2.2E+00	2.7E+05	1.5E+02
5.0E-01	3.7E+00	2.1E+00	2.9E+00	4.2E+05	1.5E+02
6.3E-01	4.3E+00	2.3E+00	3.9E+00	6.6E+05	1.4E+02

u	sm	eu	gd	yb	hf

Equilibrium Zircon Concentrations (Figure 4)

u	sm	eu	gd	yb	hf

9.9E+03	1.3E-10	1.2E-08	1.1E-04	1.4E+01	2.9E+03
4.7E+03	7.3E-08	2.0E-06	4.4E-03	6.3E+01	3.7E+03
2.9E+03	2.8E-06	3.8E-05	3.6E-02	1.4E+02	4.3E+03
2.0E+03	3.5E-05	2.8E-04	1.5E-01	2.4E+02	4.9E+03
1.5E+03	2.4E-04	1.3E-03	4.3E-01	3.4E+02	5.5E+03
1.1E+03	1.1E-03	4.3E-03	9.8E-01	4.4E+02	6.0E+03
8.8E+02	3.8E-03	1.2E-02	1.9E+00	5.4E+02	6.6E+03
7.0E+02	1.1E-02	2.7E-02	3.4E+00	6.1E+02	7.2E+03
5.7E+02	2.8E-02	5.4E-02	5.3E+00	6.7E+02	7.8E+03
4.7E+02	6.1E-02	1.0E-01	7.9E+00	7.2E+02	8.5E+03
3.9E+02	1.2E-01	1.7E-01	1.1E+01	7.5E+02	9.1E+03
3.2E+02	2.3E-01	2.7E-01	1.5E+01	7.6E+02	9.8E+03
2.7E+02	4.0E-01	4.2E-01	1.9E+01	7.6E+02	1.1E+04
2.3E+02	6.6E-01	6.0E-01	2.4E+01	7.5E+02	1.1E+04
1.9E+02	1.0E+00	8.4E-01	2.9E+01	7.3E+02	1.2E+04
1.7E+02	1.6E+00	1.1E+00	3.4E+01	7.0E+02	1.3E+04
1.4E+02	2.3E+00	1.5E+00	3.9E+01	6.7E+02	1.4E+04
1.2E+02	3.2E+00	1.9E+00	4.5E+01	6.3E+02	1.5E+04
1.0E+02	4.4E+00	2.3E+00	4.9E+01	5.9E+02	1.6E+04
9.0E+01	5.9E+00	2.8E+00	5.4E+01	5.5E+02	1.7E+04

1.0E+04	9.2E+00	1.2E-08	1.1E-04	4.8E+02	2.1E+04
4.7E+03	4.4E+00	2.0E-06	4.4E-03	2.9E+02	1.2E+04
2.9E+03	2.8E+00	3.8E-05	3.6E-02	2.8E+02	9.8E+03
2.0E+03	1.9E+00	2.8E-04	1.5E-01	3.4E+02	8.8E+03
1.5E+03	1.5E+00	1.3E-03	4.3E-01	4.2E+02	8.4E+03
1.2E+03	6.8E+00	4.3E-03	9.8E-01	7.9E+02	2.0E+04
9.2E+02	5.4E+00	1.2E-02	1.9E+00	8.1E+02	1.7E+04
7.3E+02	4.4E+00	2.7E-02	3.4E+00	8.4E+02	1.6E+04
5.9E+02	3.6E+00	5.4E-02	5.3E+00	8.6E+02	1.5E+04
4.9E+02	3.5E+00	1.0E-01	7.9E+00	8.9E+02	1.5E+04
4.1E+02	2.9E+00	1.7E-01	1.1E+01	8.9E+02	1.5E+04
3.4E+02	2.5E+00	2.7E-01	1.5E+01	8.8E+02	1.4E+04
2.8E+02	2.5E+00	4.2E-01	1.9E+01	8.7E+02	1.5E+04
2.4E+02	2.3E+00	6.0E-01	2.4E+01	8.3E+02	1.5E+04
2.0E+02	2.3E+00	8.4E-01	2.9E+01	8.0E+02	1.5E+04
1.7E+02	2.5E+00	1.1E+00	3.4E+01	7.5E+02	1.5E+04
1.5E+02	3.0E+00	1.5E+00	3.9E+01	7.0E+02	1.5E+04
1.2E+02	3.7E+00	1.9E+00	4.5E+01	6.6E+02	1.6E+04
1.1E+02	4.6E+00	2.3E+00	4.9E+01	6.0E+02	1.6E+04
9.0E+01	5.9E+00	2.8E+00	5.4E+01	5.5E+02	1.7E+04

2.7E+03	5.7E-06	2.6E-06	1.4E-02	2.4E+00	4.5E-04
1.4E+03	1.4E-04	5.6E-05	9.6E-02	9.2E+00	2.5E-02
9.6E+02	9.2E-04	3.4E-04	3.0E-01	2.0E+01	2.6E-01
7.3E+02	3.5E-03	1.2E-03	6.6E-01	3.5E+01	1.4E+00
6.0E+02	9.8E-03	3.3E-03	1.2E+00	5.4E+01	5.0E+00
5.0E+02	2.3E-02	7.5E-03	2.0E+00	7.8E+01	1.4E+01
4.4E+02	4.6E-02	1.5E-02	3.1E+00	1.0E+02	3.5E+01
3.9E+02	8.6E-02	2.7E-02	4.5E+00	1.4E+02	7.5E+01
3.5E+02	1.5E-01	4.5E-02	6.3E+00	1.7E+02	1.5E+02
3.1E+02	2.4E-01	7.2E-02	8.4E+00	2.1E+02	2.7E+02
2.9E+02	3.8E-01	1.1E-01	1.1E+01	2.5E+02	4.7E+02
2.6E+02	5.6E-01	1.6E-01	1.4E+01	3.0E+02	7.8E+02
2.5E+02	8.1E-01	2.3E-01	1.7E+01	3.5E+02	1.2E+03
2.3E+02	1.1E+00	3.2E-01	2.1E+01	4.0E+02	1.9E+03
2.1E+02	1.6E+00	4.4E-01	2.6E+01	4.6E+02	2.8E+03
2.0E+02	2.1E+00	5.8E-01	3.1E+01	5.2E+02	4.1E+03
1.9E+02	2.8E+00	7.7E-01	3.7E+01	5.8E+02	5.9E+03
1.8E+02	3.7E+00	9.9E-01	4.3E+01	6.5E+02	8.2E+03
1.7E+02	4.7E+00	1.3E+00	5.0E+01	7.2E+02	1.1E+04
1.6E+02	6.0E+00	1.6E+00	5.8E+01	8.0E+02	1.5E+04

1.8E+04	2.6E-04	1.2E-04	6.3E-01	1.1E+02	1.7E-04
8.5E+03	5.2E-03	2.1E-03	3.5E+00	3.4E+02	1.0E-02
5.2E+03	2.8E-02	1.0E-02	8.9E+00	6.1E+02	1.1E-01
3.6E+03	8.6E-02	3.0E-02	1.6E+01	8.7E+02	6.1E-01
2.7E+03	2.0E-01	6.7E-02	2.5E+01	1.1E+03	2.3E+00
2.0E+03	3.7E-01	1.2E-01	3.4E+01	1.3E+03	7.1E+00
1.6E+03	6.3E-01	2.0E-01	4.2E+01	1.4E+03	1.8E+01
1.3E+03	9.5E-01	3.0E-01	5.0E+01	1.5E+03	4.1E+01
1.0E+03	1.3E+00	4.1E-01	5.7E+01	1.5E+03	8.5E+01
8.5E+02	1.8E+00	5.3E-01	6.2E+01	1.5E+03	1.7E+02
7.0E+02	2.3E+00	6.7E-01	6.6E+01	1.5E+03	3.0E+02
5.9E+02	2.8E+00	8.1E-01	6.9E+01	1.5E+03	5.2E+02
4.9E+02	3.3E+00	9.4E-01	7.1E+01	1.4E+03	8.8E+02
4.2E+02	3.8E+00	1.1E+00	7.1E+01	1.3E+03	1.4E+03
3.5E+02	4.3E+00	1.2E+00	7.1E+01	1.2E+03	2.2E+03
3.0E+02	4.7E+00	1.3E+00	6.9E+01	1.2E+03	3.4E+03
2.6E+02	5.1E+00	1.4E+00	6.7E+01	1.1E+03	5.0E+03
2.2E+02	5.5E+00	1.5E+00	6.4E+01	9.7E+02	7.4E+03
1.9E+02	5.7E+00	1.5E+00	6.1E+01	8.8E+02	1.1E+04
1.6E+02	6.0E+00	1.6E+00	5.8E+01	8.0E+02	1.5E+04

2.9E+03	2.8E+01	2.6E-06	1.4E-02	1.4E+03	5.5E+04
1.5E+03	1.3E+01	5.6E-05	9.6E-02	6.8E+02	2.6E+04
1.0E+03	8.3E+00	3.4E-04	3.0E-01	4.4E+02	1.6E+04
7.7E+02	5.8E+00	1.2E-03	6.6E-01	3.3E+02	1.2E+04
6.3E+02	4.4E+00	3.3E-03	1.2E+00	2.8E+02	8.7E+03
5.3E+02	3.4E+00	7.5E-03	2.0E+00	2.5E+02	6.8E+03
4.5E+02	2.8E+00	1.5E-02	3.1E+00	2.4E+02	5.4E+03
4.0E+02	2.3E+00	2.7E-02	4.5E+00	2.5E+02	4.4E+03
3.6E+02	1.9E+00	4.5E-02	6.3E+00	2.6E+02	3.7E+03
3.2E+02	1.7E+00	7.2E-02	8.4E+00	2.8E+02	3.2E+03
2.9E+02	1.6E+00	1.1E-01	1.1E+01	3.1E+02	2.8E+03
2.7E+02	1.5E+00	1.6E-01	1.4E+01	3.5E+02	2.7E+03
2.5E+02	1.6E+00	2.3E-01	1.7E+01	3.9E+02	2.8E+03
2.3E+02	1.8E+00	3.2E-01	2.1E+01	4.3E+02	3.1E+03
2.2E+02	2.1E+00	4.4E-01	2.6E+01	4.8E+02	3.8E+03
2.0E+02	2.5E+00	5.8E-01	3.1E+01	5.4E+02	4.8E+03
1.9E+02	3.1E+00	7.7E-01	3.7E+01	6.0E+02	6.4E+03
1.8E+02	3.8E+00	9.9E-01	4.3E+01	6.6E+02	8.5E+03
1.7E+02	4.8E+00	1.3E+00	5.0E+01	7.3E+02	1.1E+04
1.6E+02	6.0E+00	1.6E+00	5.8E+01	8.0E+02	1.5E+04

Supplementary File 2

LA-ICP-MS Methodology

Coarse powdered rock samples were sieved to a size fraction of < 355 μm from which heavy minerals were separated by panning. Crystals were then hand-picked using a binocular microscope and set into epoxy grain mounts that were polished to 1 μm. Epoxy mounts were then coated in Au-Pd for CathodoLuminescence (CL-) images taken with a Gatan® mini-CL on the FEI Quanta 600F Scanning Electron Microscope (SEM) at the Linus Pauling Institute at OSU. Au-Pd coats were then removed by lightly polishing on 0.3 μm Al media, after which epoxy mounts were sonicated in DI.

Laser Ablation-Quadrupole-Inductively Coupled Plasma-Mass Spectrometry (LA-Q-ICP-MS)

LA-Q-ICP-MS was used to determine U-Pb dates of zircons in the Keck Collaboratory at OSU. Ablation was conducted using an Applied Spectra RESOlution-SE 193nm ArF Excimer laser with optimized settings set to 30 μm spot, 5 Hz rep rate, and 3 J•cm-2 fluence. Background and ablation durations were set to 30 seconds and 40 seconds, respectively. Measured analytes were ^{202}Hg, $^{204,206\text{-}208}$Pb, ^{232}Th, ^{235,238}U. Detection limits were calculated according to Longerich et al. (1996). Data reduction was done in LaserTRAMZ (Lewis et al., 2023) using well-known and defined procedures (Horstwood et al., 2016). ^{206}Pb/^{238}U isotope ratios were corrected for downhole laser induced elemental fractionation by application of an exponential fit (Košler et al., 2002; Paton et al., 2010), with an uncertainty determined from the standard error of the intercept. Instrumental mass fractionation was corrected for by determining a fractionation factor from the deviation of the determined age for the primary standard, Temora-2. Th-disequilibrium was accounted for by assuming constant partitioning of Th and U between zircon and melt based on the experimentally determined $D^{Th/U}$ = 0.33 (Rubatto and Hermann, 2007). Dates were calculated using the decay constants of Jaffey et al. (1971). Concordant dates were then determined by plotting unknown data on Tera-Waserburg Concordia and projecting onto Concordia from the common Pb ratios determined from plagioclase separates – the so-called ^{207}Pb method (Vermeesch, 2018; and references therein). Excess variance of the isotope ratios used for determination of ages (^{206}Pb/^{238}U and ^{207}Pb/^{206}Pb) were determined using the normalized ratios of the zircon reference material 94-35. Uncertainties associated with isotope ratios of unknowns (including excess variance), primary standard isotope ratios and accepted age, plagioclase separate $^{207}Pb/^{206}Pb$ ratios, decay constants, and long-term uncertainty of the zircon reference materials are included in the fully propagated uncertainties.

<u>Laser Ablation-Multicollector-Inductively Coupled Plasma-Mass Spectrometry (LA-MC-ICP-MS)</u>

LA-MC-ICP-MS U-Pb geochronology was also applied to zircons from the Chaxas Complex and Pre-Chaxas eruptions using the Nu Plasma 3D at OSU. The laser system and ablation parameters are the same as those described for the optimized LA-Q-ICP-MS settings. The collector block of the Nu Plasma 3D facilitates collection of ^{232}Th, ^{23}5U, and ^{238}U on Faradays, ^{202}Hg and ^{204}Pb on ion counters, and ^{206}Pb-^{208}Pb on Daly photomultipliers. Isotope ratios were reduced following largely the same protocols as described for LA-Q-ICP-MS data above with a few important exceptions. Analytical drift was observed for all sessions and was accounted for by applying a fractionation factor using the sliding window correction (Gehrels et al., 2008). Standard blocks were also measured every six unknown analyses as opposed to every 20. As with the LA-Q-ICP-MS analyses, all standards were reproduced within uncertainty.

Mixture Modeling Summary

In order to leverage both the fairly sized U-Pb dataset in this study and the precision provided by MC analyses the Expectation-Maximization algorithm (EM-algorithm) (Dempster et al., 1977) was employed. The purpose of this method is to resolve underlying (Gaussian) distributions (*k* components) that contribute to a larger distribution and is particularly useful in this instance because of the presence of both small and large uncertainties (see Figure 2 in this manuscript). Initialization was done by drawing *k* random analyses from the U-Pb data to generate an initial mean, standard deviation, and relative weights of the *k* components underlying the entire observed distribution to assign responsibilities of each of the *k* components to every analysis. Maximization was then achieved by updating the parameters of the *k* components using the standard 'update equations', which are effectively a new set of parameters weighted for the new responsibilities. Log-likelihood was then calculated and the algorithm was repeated using a convergence criteria of 1e-8 on the log-likelihood.

The EM-algorithm was slightly modified to account for the combination of large and small errors and to deal with the two critical assumptions inherent to analytical error and the EM-algorithm. First, acknowledging that some of the uncertainties are particularly large, the entire U-Pb age distribution was bootstrapped by drawing 500 random ages with replacement (xenocrysts >10Ma excluded) and a probability of drawing proportional to the inverse of the normalized uncertainties (2s; note probabilities must sum to one). When drawing an age, a random point was drawn from the width of the uncertainty assuming a gaussian distribution centered on the point estimate. Secondly, the EM-algorithm requires an assumption of *k* components upon implementation. For each sample the entire algorithm was bootstrapped 1000 times for each possible *k* value of 2-7 and the Akaike information criterion (AIC) and Bayesian information criterion (BIC) were compared for each of the components. Importantly, these information criteria penalize the addition of added components to avoid overfitting. When possible, the number of components with the lowest value in both information criterion was chosen (most likelihood after accounting for the penalty). When the standard deviation of the AIC and BIC distributions from the bootstraps overlapped, qualitative assessment was used on the resulting fit of the EM-algorithm to the data. The best fit was essentially obvious by fitting the data to the realized *k* components and assessing any severe skewness or overlap of resulting distributions and analyses once fitting the data in U-Pb space.

The resulting distribution from this GMM approach are shown immediately below. Notice that in some cases the distributions are offset from most of the data due to severely different weights associated with each dataset. Moreover, different iterations of the EM-algorithm would converge to different solutions, such that the zircon dates belonging to a particular subpopulation would shift. This ultimately resulted in skewed means, particularly if the algorithm did not frequently converge to the same result. In eruptions with evenly dispersed datasets, the algorithim also failed to reliably converge (e.g., Cerro Chaxas and MBA). As a result, the Skew-Normal mixture modeling approached was implemented using the mixsnm package in R-studio, resulting in the distributions shown in Figure 5 in this manuscript. As seen there, the distributions appropriately describe the data.

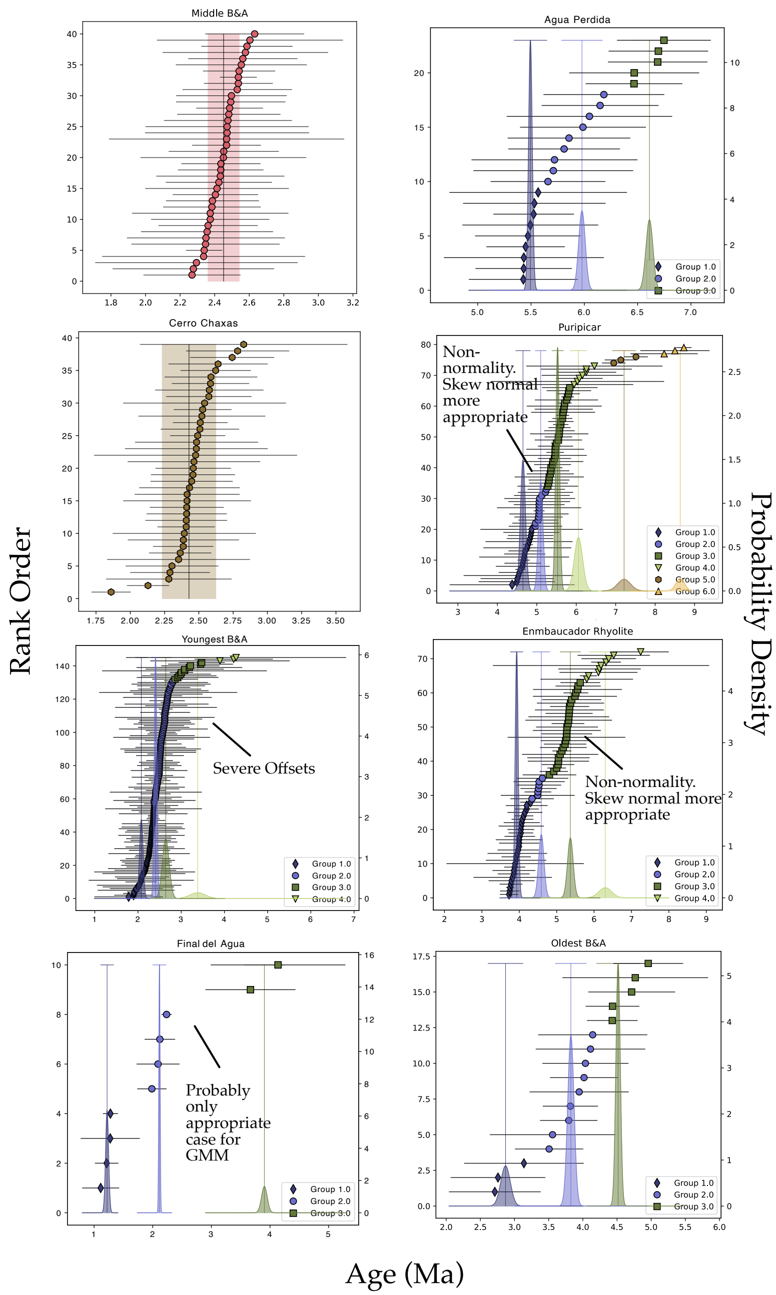

Middle B&A
Cerro Chaxas
Youngest B&A
Final del Agua
Agua Perdida
Puripicar
Enmbaucador Rhyolite
Oldest B&A
Rank Order
Probability Density
Age (Ma)
Non-normality. Skew normal more appropriate
Severe Offsets
Non-normality. Skew normal more appropriate
Probably only appropriate case for GMM
Group 1.0
Group 2.0
Group 3.0
Group 4.0
Group 5.0
Group 6.0

Thermal Modeling Summary

The MagmaThermoKinematics (MTK) software (Kaus et al., 2024) previously used to describe the modeling of zircon age spectra from thermal models (Schmitt et al., 2023) was used here using the Julia coding language in order to model synthetic zircon age spectra. For the PPI zircon age spectra, a 2D grid 70km wide by 25km deep was modeled with a resolution of 500 x 500 points over a time domain of 2.5 million years. No initial intrusion was assumed, consistent with the spacing of zircon subpopulations which suggest that resident magma was probably not present 2.5 million years before the eruption of the PPI. Prior estimates of the geotherm resulting from flare-up magmatism of the Andes estimated a geotherm of 50°C/km based on instantaneous intrusion of the entire APMB (de Silva and Gosnold, 2007). Given this and the location of the Chaxas Volcanic Complex at the edge of the APMB where thermal perturbation is not as significant an initial geotherm of 40°C / km was used. Dikes were injected at random locations into the grid within a 0.8x0.8 area relative to the grid size (i.e., a 56 x 20 km area). Each dike had a width and thickness of 5e3x0.2e3, scaling to a volume of 2.618 km^3. This intrusion area is consistent with the footprint of the Chaxas Volcanic Complex magmatic system (Lewis et al., 2025) and the depths of APVC magma storage conditions previously determined in other ignimbrites by geobarometry, mineral equilibria, and geophysics (Grocke et al., 2017; Lindsay et al., 2001; Pritchard et al., 2018) including the PPI (Abot, 2009; de Silva, 1987). Each dike carried 100 tracers that were free to move throughout the grid as subsequent dikes propagated and moved older intruded material to the side. Tracers were saved every 100 timesteps. Following each model, tracer information was saved into a jld file and subsequently reduce using previously described methodology (Weber et al., 2020) as implemented in the MTK software (Kaus et al., 2024), using a Zr-saturation range of 820 – 690 °C. MBA models were similar to the PPI except that the injection area was changed to a 10km width on a 70x20km domain, consistent with the focused extrusion of domes on the southern edge of the Chaxas Volcanic Complex (Lewis et al., 2025), and the model duration was set to 460 thousand years to roughly match the time domain recorded by MBA zircons. In order to vary the flux, the frequency of dike intrusion across the time domain was varied. The table below shows the intrusion histories assumed for the best fit models.

PPI Model Fourteen			
Model Time (kyr)	**Recharge Rate (kyr)**	**Interval Vol (km3)**	**Interval Flux (km3 / yr)**
0 - 400	1	1047.2	0.0026
400-1000	5	314.2	0.0005
1000-1300	0.5	1570.8	0.0052
1300-1800	8	163.6	0.0003
1800-2200	0.5	2094.4	0.0052
2200-2500	6	130.9	0.0004
	Time Integrated	5321.1	0.0021

MBA Model Nineteen			
Model Time (kyr)	**Recharge Rate (kyr)**	**Int. Vol (km3)**	**Int. Flux (km3 / yr)**
0-150	2	196.4	0.0013
150-460	6	135.3	0.0004
	Time Integrated	331.6	0.0007

References

Abot, M., 2009. Development of Continental Magmatic systems: Insights from Amphibole Chemistry of the Altiplano Puna Volcanic Complex, Central Andes (M.S.). Oregon State University, Corvallis, OR.

Boris Kaus, Albert de Montserrat, Pascal Aellig, 2024. boriskaus/MagmaThermoKinematics.jl: v0.5.2. https://doi.org/10.5281/ZENODO.7985281

de Silva, S., 1987. Large volume explosive volcanism in the Central Andes of N. Chile (PhD). Open University.

de Silva, S.L., Gosnold, W.D., 2007. Episodic construction of batholiths: Insights from the spatiotemporal development of an ignimbrite flare-up. Journal of Volcanology and Geothermal Research 167, 320–335. https://doi.org/10.1016/j.jvolgeores.2007.07.015

Dempster, A.P., Laird, N.M., Rubin, D.B., 1977. Maximum Likelihood from Incomplete Data Via the *EM* Algorithm. Journal of the Royal Statistical Society: Series B (Methodological) 39, 1–22. https://doi.org/10.1111/j.2517-6161.1977.tb01600.x

Gehrels, G.E., Valencia, V.A., Ruiz, J., 2008. Enhanced precision, accuracy, efficiency, and spatial resolution of U-Pb ages by laser ablation-multicollector-inductively coupled plasma-mass spectrometry: TECHNICAL BRIEF. Geochem. Geophys. Geosyst. 9, n/a-n/a. https://doi.org/10.1029/2007GC001805

Grocke, S.B., Andrews, B.J., de Silva, S.L., 2017. Experimental and petrological constraints on long-term magma dynamics and post-climactic eruptions at the Cerro Galán caldera system, NW Argentina. Journal of Volcanology and Geothermal Research 347, 296–311. https://doi.org/10.1016/j.jvolgeores.2017.09.021

Horstwood, M.S.A., Košler, J., Gehrels, G., Jackson, S.E., McLean, N.M., Paton, C., Pearson, N.J., Sircombe, K., Sylvester, P., Vermeesch, P., Bowring, J.F., Condon, D.J., Schoene, B., 2016. Community-Derived Standards for LA - ICP - MS U-(Th-)Pb Geochronology – Uncertainty Propagation, Age Interpretation and Data Reporting. Geostand Geoanal Res 40, 311–332. https://doi.org/10.1111/j.1751-908X.2016.00379.x

Jaffey, A.H., Flynn, K.F., Glendenin, L.E., Bentley, W.C., Essling, A.M., 1971. Precision Measurement of Half-Lives and Specific Activities of U 235 and U 238. Phys. Rev. C 4, 1889–1906. https://doi.org/10.1103/PhysRevC.4.1889

Košler, J., Fonneland, H., Sylvester, P., Tubrett, M., Pedersen, R.-B., 2002. U–Pb dating of detrital zircons for sediment provenance studies—a comparison of laser ablation ICPMS and SIMS techniques. Chemical Geology 182, 605–618. https://doi.org/10.1016/S0009-2541(01)00341-2

Lewis, C., de Silva, S., Cisneros De Leon, A., Burns, D., Villarroel, M., 2025. Effusive volcanic microcosm of a regional ignimbrite flare-up: Prolonged life cycle of the Chaxas Complex, northern Chile, and its influence on modern volcanic arc character. Geological Society of America Bulletin. https://doi.org/10.1130/B37909.1

Lewis, C., Kent, A., Russo, C., Lubbers, J., 2023. LaserTRAMZ. https://doi.org/10.5281/ZENODO.8097362

Lindsay, J.M., Schmitt, A.K., Trumbull, R.B., de Silva, S.L., Siebel, W., Emmermann, R., 2001. Magmatic Evolution of the La Pacana Caldera System, Central Andes, Chile: Compositional Variation of Two Cogenetic, Large-Volume Felsic Ignimbrites. Journal of Petrology 42, 459–486. https://doi.org/10.1093/petrology/42.3.459

Longerich, H.P., Jackson, S.E., Gunther, D., 1996. Laser Ablation Inductively Coupled Plasma Mass Spectrometric Transient Signal Data Acquisition and Analyte Concentration Calculation*. Journal of Analytical Atomic Spectrometry 11, 899–904.

Paton, C., Woodhead, J.D., Hellstrom, J.C., Hergt, J.M., Greig, A., Maas, R., 2010. Improved laser ablation U-Pb zircon geochronology through robust downhole fractionation

correction: IMPROVED LASER ABLATION U-Pb GEOCHRONOLOGY. Geochem. Geophys. Geosyst. 11, n/a-n/a. https://doi.org/10.1029/2009GC002618
Pritchard, M.E., de Silva, S.L., Michelfelder, G., Zandt, G., McNutt, S.R., Gottsmann, J., West, M.E., Blundy, J., Christensen, D.H., Finnegan, N.J., Minaya, E., Sparks, R.S.J., Sunagua, M., Unsworth, M.J., Alvizuri, C., Comeau, M.J., del Potro, R., Díaz, D., Diez, M., Farrell, A., Henderson, S.T., Jay, J.A., Lopez, T., Legrand, D., Naranjo, J.A., McFarlin, H., Muir, D., Perkins, J.P., Spica, Z., Wilder, A., Ward, K.M., 2018. Synthesis: PLUTONS: Investigating the relationship between pluton growth and volcanism in the Central Andes. Geosphere 14, 954–982. https://doi.org/10.1130/GES01578.1
Rubatto, D., Hermann, J., 2007. Experimental zircon/melt and zircon/garnet trace element partitioning and implications for the geochronology of crustal rocks. Chemical Geology 241, 38–61. https://doi.org/10.1016/j.chemgeo.2007.01.027
Schmitt, A.K., Sliwinski, J., Caricchi, L., Bachmann, O., Riel, N., Kaus, B.J.P., Cisneros De Léon, A., Cornet, J., Friedrichs, B., Lovera, O., Sheldrake, T., Weber, G., 2023. Zircon age spectra to quantify magma evolution. Geosphere 19, 1006–1031. https://doi.org/10.1130/GES02563.1
Vermeesch, P., 2018. IsoplotR: A free and open toolbox for geochronology. Geoscience Frontiers 9, 1479–1493. https://doi.org/10.1016/j.gsf.2018.04.001
Weber, G., Caricchi, L., Arce, J.L., Schmitt, A.K., 2020. Determining the current size and state of subvolcanic magma reservoirs. Nature Communications 11. https://doi.org/10.1038/s41467-020-19084-2